Mathematics

https://www.aimspress.com/journal/Math

AIMS Mathematics, 11(8): 27264–27303.
DOI: 10.3934/math.20261091
Received: 06 June 2026
Revised: 13 August 2026
Accepted: 19 August 2026
Published: 28 August 2026

Research article

Finite-time synchronization in uncertain switched coupled neural networks via Newton iterative hybrid control

Yongwei Yang[1,*], **Chengye Zou**[2,*] **and Hao Zhang**[3]

[1] School of Big Data and Statistics, Tongling University, Tongling 244061, China
[2] School of Artificial Intelligence, Yanshan University, Qinhuangdao 066004, China
[3] College of Computer Science and Technology, Taiyuan University of Technology, Taiyuan 030600, China

* **Correspondence:** Email: yangyw@tlu.edu.cn, zouchengye@ysu.edu.cn.

Abstract: This study addresses finite-time synchronization of coupled neural networks under uncertain switching topologies. A hybrid impulsive controller with Newton-based parameter identification is proposed to achieve rapid synchronization in randomly switching networks. The controller integrates linear control, nonlinear power-law feedback, and impulsive actions, while Newton iteration enables accelerated parameter estimation via second-order gradient information. The key innovation lies in decoupling the parameter identification from the synchronization dynamics, allowing precise estimation without topological constraints. Numerical simulations demonstrate superior convergence speed and accuracy compared with gradient descent, adaptive law, and sliding mode methods, with over 85% of tested parameter combinations achieving successful convergence, attributed to Newton's superlinear convergence and adaptive step adjustment. The framework shows strong robustness under dynamic topological changes, offering a reliable solution for time-sensitive applications in medical diagnostics and neural analysis.

Keywords: finite-time synchronization; randomly switched networks; coupled neural networks; hybrid impulsive controller
Mathematics Subject Classification: 34D06, 93C23

1. Introduction

Coupled neural networks (CNNs) characterize interactions and co-evolutionary mechanisms among neurons, revealing collective dynamic behaviors in complex systems and providing a critical theoretical foundation for understanding information processing, synchronization, and self-organization phenomena, as well as for constructing brain-inspired intelligent models. Through the collaborative operation of multiple subnetworks, CNNs have demonstrated outstanding performance across various fields. In the field of image processing, deep convolutional neural networks have achieved breakthrough progress in medical image analysis, significantly improving the accuracy of disease diagnosis [1]. In time series forecasting, researchers have developed hybrid frameworks by coupling long short-term memory (LSTM) neural networks with state-space models, enabling the capture of complex seasonal patterns and delivering exceptional performance in financial forecasting [2]. In biomedicine, graph neural networks combined with multimodal data fusion techniques, have enabled more precise brain connectivity research and neurological disease diagnoses [3]. In natural language processing, the integration of multi-embedding methods with deep learning has markedly enhanced performance in tasks such as Arabic named entity recognition [4]. These studies collectively demonstrate that coupled architectures offer effective solutions for complex tasks through collaborative learning.

In view of the collaborative advantages of CNNs across multiple domains, research on their synchronization is of paramount significance. Synchronization can optimize information transfer among subnetworks, enhancing the system's overall stability and efficiency, thereby enabling more accurate image diagnostics, more reliable time-series forecasting, deeper insights into brain connectivity, and improved performance in natural language processing tasks. Addressing synchronization challenges will strengthen the collaborative learning capability of coupled architectures for complex tasks, driving intelligent cross-domain applications toward higher precision and robustness.

In recent years, research on synchronization control of CNNs has expanded rapidly in both scope and depth, covering several core directions. In adaptive and switching control, Cao et al. [5] proposed node-edge dual-mode adaptive control for multi weight coupled networks to ensure synchronization under switching topologies, while Wang et al. [6] established unified criteria for finite-time and H_∞ synchronization of multi state/multi derivative networks. For finite/fixed-time and prescribed-time synchronization, Tang et al. [7] introduced aperiodic intermittent control for competitive neural networks and achieved fixed-time quasi-bipartite synchronization, whereas Huang et al. [8] developed a prescribed-time drive-response model with a two-layer controller enabling adjustable convergence time. In event-triggered control, Aili et al. [9] designed a time-sampling-based event-triggered controller to reduce the communication load; Zheng et al. [10] proposed a hybrid event-triggered scheme with semi-looped functionals for delayed networks; and Yi et al. [11] combined dynamic event-triggered mechanisms with impulsive control to achieve delayed synchronization while avoiding Zeno behavior. In the context of communication-efficient control, Zheng et al. [12] addressed fixed-time synchronization of discontinuous fuzzy competitive neural networks by introducing nontrivial quantized control protocols that deliberately omit the linear transmission term. Through sophisticated inequality skills combined with differential inclusion theory, they derived admirably uncomplicated synchronization criteria with effectively evaluated and less conservative settling times. Regarding fractional-order systems, Chen and Li [13] established a new Caputo inequality for discrete competitive networks, Li et al. [14] designed adaptive nonlinear controllers via the nabla Laplace transform for Cohen-Grossberg networks, and Wu et al. [15] achieved synchronization using event-dependent intermittent control with higher-order interactions and mixed delays. In memristive neural networks, Zhou et al. [16] designed tunable controllers under stochastic intermittent disturbances and applied them to image encryption, while Chang et al. [17] used particle swarm optimization to realize finite-time cluster synchronization of fractional-order complex-valued networks. For secure synchronization under attacks, Liu et al. [18] addressed random attacks via event-triggered impulsive control, Chen et al. [19] realized practical fixed-time bipartite synchronization under deception attacks using dual-channel triggering, and Si et al. [20] developed resilient sampled-data control against denial-of-service attacks. In inertial neural networks, Han et al. [21] achieved finite-time synchronization using a reduction approach and passivity theory, Cui et al. [22] extended local results to global practical synchronization via delayed impulsive control, and Ran and Zhang [23] realized stochastic fixed-time synchronization under parameter and structural mismatches. For pinning control and bipartite synchronization, Chenthamarakshan et al. [24] derived quasi-bipartite criteria for inertial networks with cooperative-competitive edges, while Dhivakaran et al. [25] addressed fractional-order memristive delayed networks under balanced and unbalanced signed graphs. In dynamic impulsive and stochastic control, Dong et al. [26] achieved almost sure synchronization of directed networks using impulsive control with randomly distributed delays. Overall, the current studies indicate a clear trend toward high-dimensional modeling, intelligent triggering mechanisms, and secure control.

Beyond the finite-time results discussed above, an even stronger notion—fixed-time stability—has recently attracted growing attention, since it guarantees a settling time with a uniform upper bound that is independent of the initial synchronization error, in contrast to finite-time convergence, whose settling time inevitably depends on the initial conditions. Along this line, Wu et al. [27] designed topology observers together with a quantized pinning controller to achieve fixed-time topology identification and synchronization for multi weighted complex networks, while Li et al. [28] proposed an adaptive fixed-time neural network control strategy in which a neural network identifies unknown system parameters and drives the tracking error to zero within a settling time that depends only on the controller parameters rather than the initial state. Zhang and Wen [29] recently established new approximate results for fixed-time stabilization of delayed inertial memristive neural networks, showing that tighter settling-time bounds can be obtained through a non reduced-order approach under event-triggered control. Recently, Ma et al. [30] established hyperbolic function-based fixed-time stability theorems for fuzzy switched Cohen-Grossberg neural networks and developed centralized and distributed controllers that furnish concise settling time estimates distinct from conventional power-law schemes. Xiong et al. [31] further extended this line by deriving limited-time stability criteria through exponential and hyperbolic cosine functions for multilayered coupled quaternion networks, designing control protocols directly in the quaternion field without resorting to power-law techniques. These observer-based and neural-network-based adaptive schemes offer a promising route toward removing the dependence of the convergence time on the initial conditions, at the cost of additional structural complexity in the controller and stability proof.

Although substantial progress has been achieved in synchronization control of CNNs, existing studies still exhibit different characteristics in terms of their analytical methods, application scenarios, and computational complexity. Adaptive and event-triggered control methods mainly rely on Lyapunov-based online parameter adjustment and are effective in reducing communication or control effort, but their convergence speed is generally limited by first-order adaptation mechanisms. Sliding mode-based approaches provide strong robustness against uncertainties; however, they usually suffer from chattering and require careful parameter tuning. Prescribed-time and fixed-time synchronization methods guarantee convergence within a predefined bound, yet most of them assume known system parameters or focus primarily on synchronization rather than simultaneous parameter identification. Furthermore, many existing parameter estimation schemes are gradient-based, resulting in relatively slow convergence and increased computational iterations for large-scale networks. In contrast, the proposed framework combines hybrid impulsive control with Newton iterative parameter identification, enabling finite-time synchronization and fast parameter estimation under uncertain switched topologies. By exploiting second-order information, the proposed method achieves faster convergence while remaining applicable to dynamically switching network structures without imposing restrictive topology assumptions.

This paper addresses the critical challenge of synchronization in CNNs under uncertain switched topologies, offering significant value for brain-inspired intelligent systems, neural connectivity analysis, and distributed information processing. By achieving reliable synchronization under dynamic topological changes—such as link failures, network reconfiguration, and adaptive routing—the proposed framework realistically reflects the typical challenges encountered in real-world neural network environments. A hybrid impulsive control strategy is introduced, which combines continuous-time regulation with discrete-time pulse correction with achieve finite-time network synchronization, offering greater flexibility compared with traditional full-network synchronization methods. Furthermore, a Newton iteration-based parameter identification approach decouples parameter estimation from synchronization dynamics, enabling accurate identification of uncertain parameters throughout the synchronization process. This method is independent of the network topology, imposes no constraints on the network's scale, and allows arbitrary topology switching, thereby demonstrating strong practical adaptability. Performance comparisons show that the proposed method significantly outperforms gradient descent, adaptive law, and sliding mode adaptive methods in terms of convergence speed, parameter identification accuracy, and synchronization error, primarily due to the superlinear convergence and automatic step-size adjustment capabilities of Newton iteration. Additionally, based on Lyapunov theory, this study rigorously proves finite-time convergence and provides an explicit expression for the convergence time, further enhancing its reliability in time-sensitive applications such as medical image diagnostics, time-series forecasting, and neurological disease diagnosis in CNN systems.

From the theoretical perspective, the main novelty of this work lies in establishing a finite-time synchronization framework that integrates Newton iterative parameter identification with hybrid impulsive control under uncertain switched topologies. A Lyapunov-based analysis is developed to rigorously prove the finite-time convergence of both synchronization errors and parameter estimation errors, while providing explicit convergence conditions for dynamically switching network topologies.

To position the proposed framework within the current state of the art, we compare it with several representative recent works. Cao et al. [5] studied multi weighted CNNs under switching topologies but provided no finite-time guarantee or parameter identification. Xi et al. [32] proposed a hybrid control strategy for finite-time synchronization, yet assumed fully known system parameters without considering uncertainty or switching topologies. Wu et al. [27] designed topology observers for fixed-time synchronization and identification, but required linear matrix inequalities feasibility, introduced additional observer complexity, and did not address uncertain nodal parameters under randomly switching structures. Yi et al. [11] combined dynamic event-triggered mechanisms with impulsive control, but restricted themselves to exponential convergence without parameter identification. Fang et al. [33] achieved finite-time synchronization via adaptive sliding mode control, yet chattering remains an inherent limitation and no parameter identification mechanism is incorporated. Dai et al. [34] proposed a finite-time convergent neural dynamics model for practical synchronization of diverse chaotic systems; although robust finite-time convergence was achieved without complex activation functions, the approach was restricted to heterogeneous drive-response systems and did not address switching network topologies or simultaneous parameter identification. In contrast, the proposed framework simultaneously achieves (i) finite-time synchronization under randomly and arbitrarily switching topologies, without imposing topological constraints or requiring LMI feasibility; (ii) decoupled Newton iterative parameter identification exploiting second-order gradient information, outperforming gradient descent and first-order adaptive laws in [5, 14, 15]; and (iii) chattering-free robustness via continuous power-law feedback combined with discrete impulsive correction. These distinctions are quantitatively validated in Section 6 (Table 1).

To make this discussion concrete, the main contributions of this paper, compared with representative existing studies, are summarized as follows.

- Faster, decoupled parameter identification. Unlike the gradient-based and adaptive-law-based identification schemes commonly used in the literature (e.g., Refs [5, 6, 14, 15]), which converge only linearly and are coupled with the synchronization error dynamics, the proposed Newton-iterative law decouples parameter identification from synchronization and exploits second-order gradient information, yielding superlinear convergence. This is confirmed quantitatively in Section 6 (Table 1), where the proposed method achieves an identification time of 11.52 s and a parameter error of 9.9858×10^{-7}, versus 13.54–18.02 s and $1.5418 \times 10^{-4} - 2.6378 \times 10^{-4}$ for the gradient descent, adaptive law, and sliding mode adaptive methods.
- Chattering-free robustness without sacrificing speed. Sliding-mode-based methods (e.g., Ref [18]) achieve robustness against uncertainty but suffer from chattering and require careful parameter tuning, as reflected in their comparatively long 18.02 s identification time. In contrast, the hybrid impulsive controller proposed here combines continuous power-law feedback with discrete impulsive correction, achieving comparable or better synchronization error (1.5247×10^{-5}) without the switching-induced chattering observed in Figure 12 (see Section 6).
- Topology-independent finite-time guarantee. Most prescribed-/fixed-time results (e.g., Refs [7, 8, 19]) either assume known system parameters or are restricted to a fixed or slowly varying topology. Our Lyapunov-based analysis instead provides an explicit finite-time convergence bound for both synchronization and parameter estimation errors that holds under arbitrary, randomly switching topologies, without imposing constraints on the network's scale.
- Quantitative, multi-baseline validation. Whereas many cited studies validate their controllers against a single baseline or through qualitative simulation only, this paper benchmarks the proposed method against three representative alternatives (gradient descent, adaptive law, and sliding mode adaptive identification) under identical 15-node switching topology conditions, directly quantifying the improvement in convergence speed, parameter accuracy, and synchronization error summarized in Table 1 (see Section 8).

2. The CNN model

To establish a rigorous foundation for our analysis, we first formalize the dynamics of a single neuron, which serves as the fundamental building block of the coupled network. The dynamic equation of an isolated neuron is described as follows:

$$\begin{aligned}\frac{d\chi(t)}{dt} &= F(\chi(t),\zeta) \\ &= \Gamma\chi(t) + f(\chi(t)) + g(\chi(t))\zeta(t),\end{aligned} \tag{2.1}$$

where $\chi(t) \in \mathbb{R}^n$ denotes the state vector of the neuron, ζ represents an unknown system parameter, and $\Gamma \in \mathbb{R}^{n\times n}$ is the coefficient matrix governing the linear dynamics of the neuron. The functions $f(\cdot)$ and $g(\cdot)$ characterize the inherent nonlinear behavior of the neuron and its dependence on the unknown parameter, respectively.

The term $\Gamma\chi(t)$ represents the intrinsic linear decay/growth of the neuron's internal state, while the term involving $f(\cdot)$ captures the parameter-dependent nonlinear self-feedback governed by the unknown parameter ζ, and the term involving $g(\cdot)$ represents an additional intrinsic nonlinearity independent of ζ. When N such neurons are interconnected, each neuron additionally receives a weighted combination of the states of its neighboring neurons, scaled by the coupling strength and the Laplacian matrix, which encodes the (possibly switching) network topology.

To provide a more intuitive understanding of the structural interactions in the network, Figure 1 illustrates the conceptual framework of a CNN, highlighting the dynamic interconnections between neurons and the effect of time-varying switching topologies—an essential feature of the system we investigate.

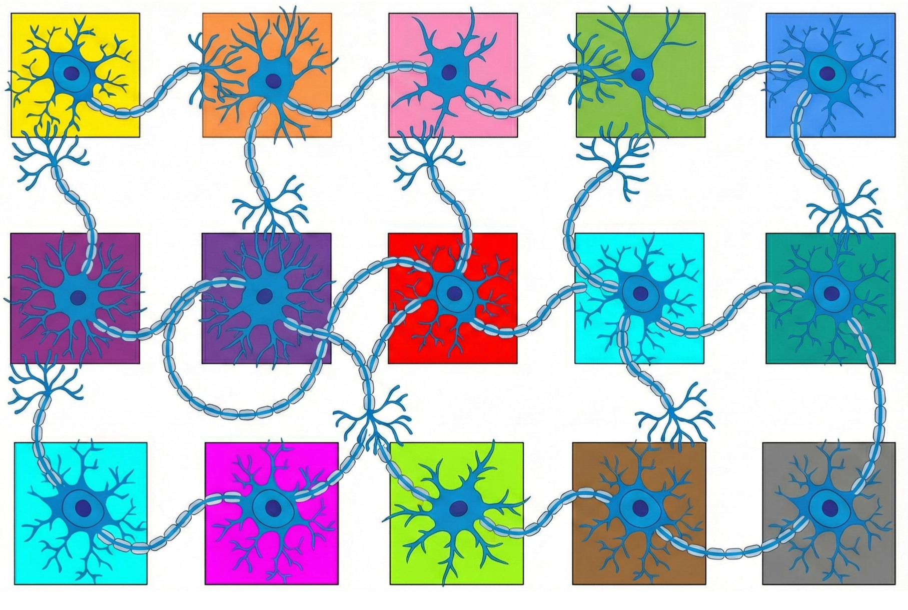

Figure 1. Conceptual diagram of a CNN.

When multiple neurons are interconnected, they form a CNN, whose collective behavior is governed by the interaction of individual neuronal dynamics. Assuming the network consists of N neurons, the dynamics of the i-th node are governed by the following:

$$\frac{d\chi_i(t)}{dt} = \Gamma\chi_i(t)+f(\chi_i(t))+g(\chi_i(t))\zeta_i(t)+\upsilon_i\sum_{j=1}^{N} q_{ij}^{\omega(t)}\chi_j(t)+g(\chi_j(t))\zeta_i(t)+U_i(t), \quad (i = 1,2,\cdots,N), \tag{2.2}$$

where

- $\upsilon_i > 0$ is the coupling strength of the i-th neuron, quantifying the influence of neighboring nodes.
- $U_i(t)$ is the external control input applied to the i-th node.
- $\zeta_i(t)$ is the online estimate of the unknown parameter associated with the i-th node, which is updated by the adaptive law (3.5) and converges to the target value $\hat{\zeta}$.
- $\omega(t) \in \{1, 2, \cdots, M\}$ is a switching signal that governs the time-varying network topology.
- $$Q^{\omega(t)} = (q_{ij}^{\omega(t)})_{N\times N}$$
  is the Laplacian matrix representing the topological structure of the network at time t. Specifically, $q_{ij}^{\omega(t)} = 1$ if there is a direct connection from node j to node i at time t, and $q_{ij}^{\omega(t)} = 0$ otherwise. The diagonal elements are defined as
  $$q_{ii}^{\omega(t)} = -\sum_{\substack{j=1\\ j\neq i}}^{N} q_{ij}^{\omega(t)}$$
  to ensure the Laplacian matrix property.

To achieve synchronization, we define a target system that represents the desired collective behavior of the entire network. Intuitively, this target system is what each node's dynamics would reduce to if the coupling and control terms in Eq (2.2) were absent and the parameter estimate were exact, i.e., it is the "ideal" trajectory that every node is asked to track. The synchronization target neuron is assumed to follow the dynamics:

$$\frac{dy(t)}{dt} = F(y(t), \hat{\zeta}) = \Gamma y(t) + f(y(t)) + g(y(t))\hat{\zeta}, \tag{2.3}$$

where $y(t) \in \mathbb{R}^q$ is the state vector of the target neuron; $\Gamma \in \mathbb{R}^{q\times q}$ is the constant matrix characterizing the linear part of the neuronal dynamics, identical to that appearing in the Eq (2.2); $f(\cdot) : \mathbb{R}^q \to \mathbb{R}^q$ is the nonlinear activation function and $g(\cdot) : \mathbb{R}^q \to \mathbb{R}^{q\times m}$ is the parameter-dependent nonlinear function, both shared with the Eq (2.2); and $\hat{\zeta} \in \mathbb{R}^m$ is the known parameter of the target system, which remains fixed throughout the synchronization process and serves as the reference value toward which the unknown nodal parameter $\zeta_i(t)$ of each response neuron converges via the Eq (3.5). In contrast to the unknown $\zeta_i(t)$ in Eq (2.2), $\hat{\zeta}$ is assumed to be precisely known and is used both to drive the target dynamics and to construct the parameter estimation error $\hat{\zeta} - \zeta_i(t)$ in the Eq (4.1).

Finally, to quantify the deviation of each neuron from the target behavior, we define the synchronization error as

$$e_i(t) = y(t) - \chi_i(t). \tag{2.4}$$

With this definition, "synchronization" simply means driving $e_i(t)$ to zero for every node i, and doing so in finite time rather than only asymptotically.

3. Controller design and adaptive law

To achieve finite-time synchronization of the CNN with uncertain parameters and switching topologies, we propose a hybrid impulsive control strategy that integrates continuous-time feedback control with discrete impulsive corrections. This controller is designed to balance rapid error suppression (via continuous control) and robust disturbance rejection (via impulsive actions), and its mathematical formulation is given by the following:

$$U_i(t) = \begin{cases} -\Upsilon e_i(t) - \beta \mathrm{sign}(e_i(t)) \, |e_i(t)|^{\alpha}, & t \neq t_r, \\ K e_i(t_r^-), & t = t_r, \end{cases} \tag{3.1}$$

where

- $\Upsilon > 0$ denotes the linear control gain, which is responsible for regulating the asymptotic convergence rate of the synchronization error.
- $\beta > 0$ is the nonlinear control gain, which accelerates error reduction in the finite-time regime.
- $\alpha \in (0, 1)$ is the power-law parameter that shapes the nonlinear feedback characteristic. Because $\alpha < 1$, the term $|e_i(t)|^{\alpha}$ grows more slowly than $|e_i(t)|$ for large errors but, crucially, decays more slowly than $|e_i(t)|$ as $e_i(t) \to 0$; this is precisely the mechanism that produces finite-time rather than only asymptotic convergence.
- $K \in \mathbb{R}^{q \times q}$ represents the impulsive gain matrix, governing the magnitude of state corrections at discrete impulsive instants $\{t_r\}$.
- The sequence $\{t_r\}$ denotes the impulsive instants, with the inter-impulse interval constrained by

$$t_{r+1} - t_r \leq \tau_{\max}$$

  (where $\tau_{\max}$ is the maximum allowable interval) to ensure control effectiveness.

Remark 3.1. *In an electronic emulation of the node dynamics* (2.1)*, the continuous term, consisting of the linear component and the power-law's nonlinear component, can be implemented with a standard operational-amplifier feedback circuit followed by a nonlinear shaping stage (e.g., a piecewise-linear or logarithmic amplifier network approximating the fractional power-law characteristic), whose output is injected as an external current into the node in the same way as the coupling and self-feedback terms already enter Eq (2.2). The impulsive component, governed by the gain matrix K and the instants* $\{t_r\}$*, corresponds to a brief, large-amplitude state correction and can be realized with a sample-and-hold/switched-capacitor circuit, or in a digital implementation with a microcontroller or field-programmable gate array that computes the required correction from sampled error measurements and delivers it as a short current or voltage pulse through a digital-to-analog converter. Such a hybrid continuous plus pulsed actuation architecture parallels existing closed-loop neurostimulation and neuromorphic circuit implementations, where continuous feedback and discrete corrective pulses are delivered to a physical or emulated neuron through the same electrode or injection port. A full hardware/circuit-level validation of the proposed controller lies beyond the theoretical scope of the present paper and is left as a direction for future work.*

In addition to the hybrid impulsive controller, accurate identification of the unknown parameter $\zeta_i(t)$ is critical for achieving precise synchronization, since both the controller and the synchronization error itself depend on how close $\zeta_i(t)$ is to the true value $\hat{\zeta}$. To this end, we adopt the Newton iteration method for adaptive parameter estimation.

We first define a cost function that penalizes both sources of error we care about—the synchronization error and the parameter estimation error—and then derive the update law as the (negative) Newton step on that cost function; the two steps below make this derivation explicit rather

than stating the final law directly.
Step 1: Cost function. Define

$$\Xi_i(e_i(t), \zeta_i(t)) = \tau e_i^{\mathrm{T}}(t)e_i(t) + \xi(\hat{\zeta} - \zeta_i(t))^{\mathrm{T}}(\hat{\zeta} - \zeta_i(t)), \tag{3.2}$$

where the positive scalars τ and ξ represent the synchronization error weight and the parameter error weight, respectively. The first term of Ξ_i penalizes a large synchronization error, while the second penalizes a parameter estimate that is far from $\hat{\zeta}$; minimizing Ξ_i therefore drives both errors toward zero simultaneously.
Step 2: Newton update law. The adaptive update law for the unknown parameter $\zeta_i(t)$ is obtained by applying Newton's method to Ξ_i with respect to $\zeta_i(t)$ as follows:

$$\frac{d\zeta_i(t)}{dt} = -\kappa \frac{\Xi_i(e_i(t),\ \zeta_i(t))}{\frac{\partial \Xi_i(e_i(t),\, \zeta_i(t))}{\partial \zeta_i(t)}}, \tag{3.3}$$

where the positive scalars κ represents the adaptation rate.
Step 3: Closed-form simplification. To make Eq (3.3) usable in practice, we need an explicit expression for the denominator. Differentiating Eq (3.2) with respect to $\zeta_i(t)$ gives

$$\frac{\partial \Xi_i(e_i(t), \zeta_i(t))}{\partial \zeta_i(t)} = -2\xi(\hat{\zeta} - \zeta_i(t)). \tag{3.4}$$

Substituting Eq (3.4) back into Eq (3.3) yields the closed-form update law

$$\frac{d\zeta_i(t)}{dt} = \frac{\kappa}{2\xi} \times \frac{\Xi_i(e_i(t), \zeta_i(t))}{\hat{\zeta} - \zeta_i(t)}. \tag{3.5}$$

This simplified update law retains the superlinear convergence property of Newton's method while reducing computational complexity—evaluating Eq (3.5) only requires Ξ_i and the current parameter gap $\hat{\zeta} - \zeta_i(t)$, with no further differentiation needed at each time step—making it suitable for real-time parameter identification in dynamic neural networks.

4. Main results

To rigorously prove the finite-time synchronization of the CNN with uncertain parameters and switching topologies, we first define a Lyapunov function that synthesizes the synchronization error and parameter estimation error, and then present the necessary assumptions and lemmas for the subsequent theoretical analysis.

Define a composite Lyapunov function $V(t)$ for the closed-loop system as follows:

$$V(t) = \frac{1}{2}\sum_{i=1}^{N} e_i^{\mathrm{T}}(t)Pe_i(t) + \frac{1}{2}\sum_{i=1}^{N} (\hat{\zeta} - \zeta_i(t))^{\mathrm{T}}(\hat{\zeta} - \zeta_i(t)), \tag{4.1}$$

where $P = \mathrm{diag}(p_1, p_2, \cdots, p_q) > 0$ is a positive definite diagonal matrix, the first term quantifies the global synchronization error of the network, and the second term characterizes the cumulative parameter estimation error of all nodes.

Since $P = \text{diag}(p_1, \ldots, p_q) > 0$ is diagonal but the coefficient matrix $\Gamma \in \mathbb{R}^{n\times n}$ appearing in Eq (2.1) is, in general, not symmetric, we introduce

$$\Gamma_s := \frac{\Gamma + \Gamma^{\mathrm{T}}}{2}, \tag{4.2}$$

the symmetric part of Γ, and let $\lambda_{\max}(\Gamma_s) \in \mathbb{R}$ denote its largest eigenvalue. Since Γ_s is real symmetric, $\lambda_{\max}(\Gamma_s)$ is a well-defined real scalar, and for any $e \in \mathbb{R}^q$, we have

$$e^{\mathrm{T}} P\Gamma e \leq \lambda_{\max}(\Gamma_s)\, e^{\mathrm{T}} Pe. \tag{4.3}$$

4.1. Assumptions and lemmas

The following assumptions and lemmas are fundamental to the proof of the finite-time synchronization theorem, where the assumptions impose mild constraints on the nonlinear characteristics of the neural network, and the lemmas provide key inequality tools for the Lyapunov function derivation.

Assumption 4.1 (Lipschitz condition [26])**.** *The nonlinear activation function $f(\cdot)$ of the neuron satisfies the global Lipschitz condition, i.e., there is a non-negative constant ϵ such that for any state vectors $y(t)$ and $\chi_i(t)$, the following inequality holds:*

$$|f(y(t)) - f(\chi_i(t))| \leq \epsilon\, |y(t) - \chi_i(t)| = \epsilon\, |e_i(t)|\,. \tag{4.4}$$

Along any trajectory of Eq (3.3), the estimation error $\hat{\zeta} - \zeta_i(t)$ satisfies

$$\begin{aligned}
\frac{d}{dt}\left[\frac{1}{2}(\hat{\zeta} - \zeta_i(t))^{\mathrm{T}}(\hat{\zeta} - \zeta_i(t))\right] &= -\frac{\kappa}{2\xi}\,\Xi_i(e_i(t), \zeta_i(t)) \\
&= -\frac{\kappa\tau}{2\xi}\, e_i^{\mathrm{T}}(t)e_i(t) - \frac{\kappa}{2}(\hat{\zeta} - \zeta_i(t))^{\mathrm{T}}(\hat{\zeta} - \zeta_i(t)) \\
&\leq -\kappa \cdot \frac{1}{2}(\hat{\zeta} - \zeta_i(t))^{\mathrm{T}}(\hat{\zeta} - \zeta_i(t)),
\end{aligned} \tag{4.5}$$

since $\Xi_i(\cdot) \geq 0$ and the synchronization error term $\tau e_i^{\mathrm{T}}(t)e_i(t)$ can only strengthen the inequality when discarded. By the comparison lemma, this yields the closed-form estimate

$$\|\hat{\zeta} - \zeta_i(t)\| \leq \|\hat{\zeta} - \zeta_i(0)\| e^{-\kappa t/2}, \quad \text{for all } t \geq 0. \tag{4.6}$$

Since the right-hand side of inequality (4.6) depends only on the target value $\hat{\zeta}$ and the user-specified initial guess $\zeta_i(0)$, inequality (4.6) shows that $\zeta_i(t)$ remains, for all $t \geq 0$, inside the compact ball, which is known a priori

$$\Omega_i := \{\zeta : \|\hat{\zeta} - \zeta\| \leq \rho_i\}, \quad \rho_i := \|\hat{\zeta} - \zeta_i(0)\|. \tag{4.7}$$

This set is fixed by design choices made before the controller is run and does not depend on the (uncertain) synchronization error trajectory or on which topology is active at time.

Assumption 4.2 ([35])**.** *(i) The target trajectory $y(t)$ of Eq (2.3) evolves within a compact absorbing set $\mathcal{Y}$, a standard dissipativity property of FitzHugh-Nagumo-type neurons that is verified directly from the isolated neuron dynamics of Eq (2.1) and does not depend on ζ; and (ii) the parameter-dependent nonlinear function $g(\cdot)$ is Lipschitz on $\mathcal{Y}$ with a constant L_g, and bounded there by $M_g = \sup_{\chi\in\mathcal{Y}} \|g(\chi)\|$.*

Using the a priori invariant set Ω_i from Eq (4.7), decompose

$$g(y(t))\hat{\zeta} - g(\chi_i(t))\zeta_i(t) = [g(y(t)) - g(\chi_i(t))]\hat{\zeta} + g(\chi_i(t))[\hat{\zeta} - \zeta_i(t)] \\ =: \vartheta_i(t)e_i(t). \tag{4.8}$$

The first term is bounded by $L_g\|\hat{\zeta}\|\|e_i(t)\|$ via the Lipschitz property in (ii); the second is bounded, via Eqs (4.6) and (4.7), by $M_g\rho_i e^{-\kappa t/2}$. Hence, $\vartheta_i(t)$ is bounded for all $t \geq 0$, with

$$\Lambda := \max\{\Phi_1, \Phi_2, \ldots, \Phi_N\}, \quad \Phi_i = \sup_{t\geq 0} |\vartheta_i(t)| \leq L_g\|\hat{\zeta}\| + M_g\rho_i. \tag{4.9}$$

So that Λ is bounded above by $L_g\|\hat{\zeta}\| + M_g \max_i \rho_i$, a quantity that is computable before the controller is implemented from known structural constants (L_g, M_g, the size of $\mathcal{Y}$) and the designer-chosen initial guesses $\zeta_i(0)$, rather than from any unknown closed-loop quantity.

Lemma 4.1 ([36]). *For any vector $e = [e_1, e_2, \cdots, e_q]^T \in \mathbb{R}^q$ and power parameter $\alpha \in (0, 1)$, the following power inequality holds:*

$$\sum_{j=1}^{q} \left|e_j\right|^{1+\alpha} \geq \left(\sum_{j=1}^{q} e_j^2\right)^{\frac{1+\alpha}{2}}. \tag{4.10}$$

Lemma 4.2 ([37]). *For a positive definite diagonal matrix $P = \mathrm{diag}(p_1, p_2, \cdots, p_q)$, let*

$$p_{\min} = \min\{p_1, p_2, \cdots, p_q\} \quad \text{and} \quad p_{\max} = \max\{p_1, p_2, \cdots, p_q\}$$

denote the minimum and maximum diagonal elements of P, respectively. Then for any vector $e \in \mathbb{R}^q$, the following norm inequality holds:

$$p_{\min} \|e\|^2 \leq e^T Pe \leq p_{\max} \|e\|^2. \tag{4.11}$$

Lemma 4.3 ([38]). *Consider the impulsive nonlinear system described by*

$$\begin{cases} \dot{V}(t) \leq \alpha_1 V(t) - \alpha_2 V^q(t), & t \neq t_r, \\ V(t_r) \leq V^{\frac{1}{1-q}} V(t_r^-), & t = t_r, \end{cases} \tag{4.12}$$

where $\alpha_1 < 0$, $\alpha_2 > 0$, $q \in (0, 1)$, and the impulsive instants satisfy $t_{r+1} - t_r \leq \tau_{\max}$. Define

$$\gamma = \mu e^{\alpha_1(1-q)\tau_{\max}}, \quad \theta = \frac{\alpha_2}{|\alpha_1|}, \quad \epsilon_0 = 1 - \left(\frac{\mu - 1}{\ln \mu}\right)\iota, \quad T_0 = \frac{2}{|\alpha_1|(1 - q)} \ln(1 - \epsilon_0),$$

where $\mu = \nu^{\frac{2}{1-\alpha}}$, and $\nu \in (0, 1)$ is the impulsive contraction coefficient. Then the system state $V(t)$ converges to zero in finite time T, where we find the following cases.

- *Case 1: If*

$$V(t_0) \leq (\epsilon_0\theta)^{\frac{1}{1-q}},$$

then $r_0 = 0$ and $T = T_0$.

- *Case 2: If*
$$V(t_0) > (\epsilon_0\theta)^{\frac{1}{1-q}}$$
and $\gamma = 1$, *then*
$$r_0 = \left\lfloor \frac{V^{1-q}(t_0) - \epsilon_0\theta}{\theta(1-\mu)} \right\rfloor + 1$$
and $T = r_0\tau_{\max} + T_0$.
- *Case 3: If*
$$(\epsilon_0\theta)^{\frac{1}{1-q}} \ll V(t_0) < \chi^*$$
and $\gamma \neq 1$, *then*
$$r_0 = \left\lfloor \log_\gamma \frac{\left(\frac{\gamma-\mu}{1-\gamma} + \epsilon_0\right)\theta}{\frac{\gamma-\mu}{1-\gamma}\theta + V^{1-q}(t_0)} \right\rfloor + 1$$
and $T = r_0\tau_{\max} + T_0$.

Here, χ^* *is a positive constant related to the system parameters, defined as* $\chi^* = \left(\frac{\mu\theta}{\mu-1}\right)^{\frac{1}{1-q}}$, *and* $\lfloor\cdot\rfloor$ *denotes the floor function.*

4.2. Finite-time synchronization theorem

On the basis of the assumptions and lemmas above, we present the main finite-time synchronization theorem for the CNN under the proposed hybrid impulsive controller and Newton iterative parameter identification law.

Theorem 4.4. *Consider the CNN system (2.2) and the target synchronization system (2.3). Under Assumptions 4.1 and 4.2 and the hybrid impulsive controller given by Eq (3.1), if the following three conditions are satisfied simultaneously:*

$$\begin{cases} \Upsilon > \lambda_{\max}(\Gamma_s) + \epsilon + \nu_i\lambda_i^{\omega(t)} + \Lambda + \kappa\xi\tau, \\ (I+K)^T P(I+K) \leq \nu^{\frac{2}{1-\alpha}} P, \\ t_{r+1} - t_r \leq \tau_{\max}, \end{cases} \tag{4.13}$$

where $\nu \in (0,1)$, $\lambda_i^{\omega(t)}$ *is the i-th eigenvalue of the Laplacian matrix corresponding to the switching topology* $\omega(t)$, *and all other parameters are defined as before. Then the network system achieves global finite-time synchronization, i.e., the synchronization error satisfies*

$$\lim_{t\to T} \|e_i(t)\| = 0 \quad \text{for all } i = 1, 2, \cdots, N$$

with a finite convergence time T, *whose explicit expression is given in Remark 4.5.*

Proof. The proof of finite-time synchronization is divided into two sequential stages: The continuous-time interval ($t \neq t_r$, no impulsive control action) and the impulsive instant ($t = t_r$, discrete impulsive state correction). We analyze the time derivative of the Lyapunov function $V(t)$ in the continuous stage and the jump characteristic of $V(t)$ at impulsive instants, then combine the two stages and apply Lemma 4.3 to prove the finite-time convergence.

Stage 1: Continuous-time intervals ($t \neq t_r$).

We first compute the time derivative of $V(t)$ along the trajectories of System (2.2). Differentiating Eq (4.1) term by term, we have

$$\frac{dV(t)}{dt} = \sum_{i=1}^{N} e_i^{\mathrm{T}}(t) P \dot{e}_i(t) - \sum_{i=1}^{N} \left(\hat{\zeta} - \zeta_i(t)\right)^{\mathrm{T}} \frac{d\zeta_i(t)}{dt}. \tag{4.14}$$

To evaluate $\dot{e}_i(t)$, recall that $e_i(t) = y(t) - \chi_i(t)$, so $\dot{e}_i(t) = \dot{y}(t) - \dot{\chi}_i(t)$; substituting the right-hand sides of Eqs (2.2) and (2.3) for $\dot{\chi}_i(t)$ and $\dot{y}(t)$, respectively, gives

$$\begin{aligned} \dot{e}_i(t) = \Gamma e_i(t) + [f(y(t)) - f(\chi_i(t))] + v_i \sum_{j=1}^{N} q_{ij}^{\omega(t)} y(t) - v_i \sum_{j=1}^{N} q_{ij}^{\omega(t)} \chi_j(t) \\ + [g(y(t))\hat{\zeta} - g(\chi_i(t))\zeta_i(t)] - U_i(t). \end{aligned} \tag{4.15}$$

The next simplification uses the row-sum-zero property of the Laplacian noted in Section 4.1: Since

$$\sum_{j=1}^{N} q_{ij}^{\omega(t)} = 0$$

for every i, and $y(t)$ does not depend on j, we have

$$\sum_{j=1}^{N} q_{ij}^{\omega(t)} y(t) = y(t) \sum_{j=1}^{N} q_{ij}^{\omega(t)} = 0, \tag{4.16}$$

so the first coupling term in Eq (4.15) drops out entirely, leaving only the coupling term in $\chi_j(t)$. Combining (4.14) and (4.15) reproduces the expanded form of $dV(t)/dt$ given in (4.15).

$$\begin{aligned} \frac{dV(t)}{dt} = \sum_{i=1}^{N} e_i^{\mathrm{T}}(t)\, P \Big[\Gamma\, e_i(t) + f(y(t)) - f(\chi_i(t)) - v_i \sum_{j=1}^{N} q_{ij}^{\omega(t)} x_j(t) \\ + g(y(t))\,\hat{\zeta} - g(\chi_i(t))\,\zeta_i(t) - U_i(t)\Big] - \sum_{i=1}^{N} \left(\hat{\zeta} - \zeta_i(t)\right)^{\mathrm{T}} \frac{d\zeta_i(t)}{dt}. \end{aligned} \tag{4.17}$$

We now bound each bracketed term in Eq (4.17) using the assumptions introduced in Section 4.1.

- Since P is is diagonally positive-definite, by Eq (4.3) the linear term $e_i^{\mathrm{T}} P \Gamma e_i(t)$ satisfies

  $$e_i^{\mathrm{T}} P \Gamma e_i(t) \leq \lambda_{\max}(\Gamma_s) e_i^{\mathrm{T}} P e_i(t),$$

  so this term contributes at most $\lambda_{\max}(\Gamma_s)$ to the coefficient of $e_i^{\mathrm{T}} P e_i(t)$.
- By Assumption 4.1,

  $$\|f(y(t)) - f(\chi_i(t))\| \leq \epsilon \|e_i(t)\|,$$

  so this term contributes at most ϵ to the coefficient of $e_i^{\mathrm{T}}(t) P e_i(t)$.

- Using the Laplacian eigenvalue relation

$$-v_i \sum_{j=1}^{N} q_{ij}^{\omega(t)} \chi_j(t) = v_i \lambda_i^{\omega(t)} \chi_i(t),$$

this coupling term contributes $v_i \lambda_i^{\omega(t)}$.
- By Assumption 4.2,

$$g(y(t))\hat{\zeta} - g(\chi_i(t))\zeta_i(t) = \vartheta_i(t) e_i(t) \quad \text{with } |\vartheta_i(t)| \leq \Lambda,$$

so this term contributes at most Λ.
- Substituting the continuous-time part of the controller (3.1),

$$U_i(t) = -\Upsilon e_i(t) - \beta\, \mathrm{sign}(e_i(t))|e_i(t)|^{\alpha},$$

contributes $-\Upsilon$ together with the nonlinear damping term.

Collecting these four contributions gives the upper bound stated as (4.18) below:

$$\begin{aligned} \frac{dV(t)}{dt} \leq & \sum_{i=1}^{N} e_i^{\mathrm{T}} P e_i(t) [\lambda_{\max}(\Gamma_s) + \epsilon + v_i \lambda_i^{\omega(t)} + \Lambda] \\ & - \sum_{i=1}^{N} e_i^{\mathrm{T}} P \Upsilon e_i(t) - \beta \sum_{i=1}^{N} \mathrm{sign}^{\mathrm{T}}(e_i(t))\, P\, e_i(t)\ |e_i(t)|^{\alpha} \\ & - \sum_{i=1}^{N} \left(\hat{\zeta} - \zeta_i(t)\right)^{\mathrm{T}} \frac{d\zeta_i(t)}{dt}. \end{aligned} \tag{4.18}$$

Next, we substitute the parameter update law itself. Using Eqs (3.2) and (3.3), the last sum in Eq (4.18) becomes

$$\frac{\kappa}{2\xi} \sum_{i=1}^{N} \Xi_i(e_i(t), \zeta_i(t)),$$

after this substitution and expanding Ξ_i as defined in Eq (3.3), we obtain

$$\begin{aligned} \frac{dV(t)}{dt} \leq & \sum_{i=1}^{N} e_i^{\mathrm{T}} P e_i(t) [\lambda_{\max}(\Gamma_s) + \epsilon + v_i \lambda_i^{\omega(t)} + \Lambda - \Upsilon] \\ & - \beta \sum_{i=1}^{N} \mathrm{sign}^{\mathrm{T}}(e_i(t))\ P\, e_i(t)\, |e_i(t)|^{\alpha} \\ & - \frac{\kappa}{2\xi} \sum_{i=1}^{N} \Xi_i(e_i(t),\ \zeta_i(t)). \end{aligned} \tag{4.19}$$

Because Ξ_i in Eq (3.2) contains both an e_i-term ($\tau e_i^{\mathrm{T}} e_i$) and a ζ_i-term, and we only need a bound rather than an exact expression, we discard the (non-negative) synchronization error part of Ξ_i and keep only the parameter estimation error part; this is a one-directional inequality, so it is still valid as an upper bound. This gives Eq (4.20) as follows:

$$\begin{aligned}\frac{dV(t)}{dt} \leq & \sum_{i=1}^{N} e_i^{\mathrm{T}} P e_i(t)[\lambda_{\max}(\Gamma_s) + \epsilon + v_i \lambda_i^{\omega(t)} + \Lambda - \Upsilon] \\ & - \beta \sum_{i=1}^{N} \mathrm{sign}^{\mathrm{T}}(e_i(t))\, P e_i(t)\, |e_i(t)|^{\alpha} \\ & - \frac{\kappa}{2\xi} \sum_{i=1}^{N} (\hat{\zeta} - \zeta_i(t))^{\mathrm{T}} (\hat{\zeta} - \zeta_i(t)).\end{aligned} \tag{4.20}$$

The first condition of Theorem 4.4 is designed precisely so that the bracketed coefficient above becomes strictly negative once we subtract $\kappa\xi\tau$ from it (the weight $\kappa\xi\tau$ appears because of how τ enters Ξ_i): writing this out explicitly gives Eq (4.21), as shown below:

$$\begin{aligned}\frac{dV(t)}{dt} \leq & \sum_{i=1}^{N} e_i^{\mathrm{T}} P e_i(t)[\lambda_{\max}(\Gamma_s) + \epsilon + v_i \lambda_i^{\omega(t)} + \Lambda - \Upsilon - \kappa\xi\tau] \\ & - \beta \sum_{i=1}^{N} \mathrm{sign}^{\mathrm{T}}(e_i(t))\, P e_i(t)\, |e_i(t)|^{\alpha} \\ & - \frac{\kappa}{2\xi} \sum_{i=1}^{N} (\hat{\zeta} - \zeta_i(t))^{\mathrm{T}} (\hat{\zeta} - \zeta_i(t)).\end{aligned} \tag{4.21}$$

Since the last term of Eq (4.21) is a sum of squares (and hence is non positive after the leading minus sign), it can only help convergence: Dropping it gives a valid, slightly more conservative upper bound (Eq (4.22)) as follows:

$$\frac{dV(t)}{dt} \leq \sum_{i=1}^{N} e_i^{\mathrm{T}} P e_i(t)[\lambda_{\max}(\Gamma_s) + \epsilon + v_i \lambda_i^{\omega(t)} + \Lambda - \Upsilon - \kappa\xi\tau] - \beta \sum_{i=1}^{N} \mathrm{sign}^{\mathrm{T}}(e_i(t))\, P e_i(t)\, |e_i(t)|^{\alpha}. \tag{4.22}$$

At this point, the linear part of the bound (the first sum) is already in a convenient quadratic form, but the nonlinear part (the second sum) is not yet comparable with $V(t)$ itself. The next two steps convert it into a power of $V_1(t)$ using Lemmas 4.1 and 4.2. By Lemma 4.1 (power inequality, applied entrywise to $e_i(t)$), we have

$$\sum_{i=1}^{N} \mathrm{sign}^{\mathrm{T}}(e_i(t))\, P e_i(t)\; |e_i(t)|^{\alpha} \geq p_{\min} \sum_{i=1}^{N} |e_i(t)|^{1+\alpha} \geq p_{\min} \left(\sum_{i=1}^{N} e_i^{\mathrm{T}}(t) e_i(t) \right)^{\frac{1+\alpha}{2}}. \tag{4.23}$$

By Lemma 4.2 (norm inequality, used here to convert the Euclidean norm back into the P-weighted norm that appears in $V(t)$), we have

$$\left(\sum_{i=1}^{N} e_i^{\mathrm{T}}(t) e_i(t) \right)^{\frac{1+\alpha}{2}} \geq \frac{1}{p_{\max}^{\frac{1+\alpha}{2}}} \left(\sum_{i=1}^{N} e_i^{\mathrm{T}}(t) P e_i(t) \right)^{\frac{1+\alpha}{2}}. \tag{4.24}$$

Chaining Eqs (4.23) and (4.24) gives

$$\sum_{i=1}^{N} \operatorname{sign}^{\mathrm{T}}(e_i(t))\, P e_i(t)\, |e_i(t)|^{\alpha} \geq \frac{p_{\min}}{p_{\max}^{\frac{1+\alpha}{2}}} \left(\sum_{i=1}^{N} e_i^{\mathrm{T}}(t) P e_i(t) \right)^{\frac{1+\alpha}{2}}. \tag{4.25}$$

Now we define

$$V_1(t) = \frac{1}{2} \sum_{i} e_i^{\mathrm{T}}(t) P e_i(t),$$

the synchronization-error half of the Lyapunov function; note that $V_1(t) \leq V(t)$ since $V(t)$ also includes the non-negative parameter error term. Substituting Eq (4.25) into Eq (4.22) and rewriting in terms of $V_1(t)$ gives

$$\begin{aligned} \frac{dV(t)}{dt} &\leq \frac{2}{p_{\min}} \left[\lambda_{\max}(\Gamma_s) + \epsilon + \nu_i \lambda_i^{\omega(t)} + \Lambda - \Upsilon - \kappa\xi\tau\right] V_1(t) - \frac{2\beta p_{\min}}{p_{\max}^{\frac{1+\alpha}{2}}} V_1^{\frac{1+\alpha}{2}}(t) \\ &= \frac{2}{p_{\min}} \Big[\lambda_{\max}(\Gamma_s) + \epsilon + \nu_i \lambda_i^{\omega(t)} + \Lambda - \Upsilon - \kappa\xi\tau\Big] \frac{V_1(t)}{V(t)} V(t) - \frac{2\beta p_{\min}}{p_{\max}^{\frac{1+\alpha}{2}}} \left(\frac{V_1(t)}{V(t)}\right)^{\frac{1+\alpha}{2}} V^{\frac{1+\alpha}{2}}(t). \end{aligned} \tag{4.26}$$

Because $0 \leq V_1(t) \leq V(t)$, it is obvious that

$$0 < \frac{V_1(t)}{V(t)} \leq 1, \quad \text{and} \quad 0 < \left(\frac{V_1(t)}{V(t)}\right)^{\frac{1+\alpha}{2}} \leq 1.$$

Equation (4.26) can be simplified to the following form:

$$\frac{dV(t)}{dt} \leq \alpha_1' V(t) - \alpha_2' V^{\frac{1+\alpha}{2}}(t), \tag{4.27}$$

where

$$\begin{aligned} \alpha_1' &= \frac{2}{p_{\min}} \frac{V_1(t)}{V(t)} \Big[\lambda_{\max}(\Gamma_s) + \epsilon + \nu_i \lambda_i^{\omega(t)} + \Lambda - \Upsilon - \kappa\xi\tau\Big] < 0, \\ \alpha_2' &= \frac{2\beta p_{\min}}{p_{\max}^{\frac{1+\alpha}{2}}} \left(\frac{V_1(t)}{V(t)}\right)^{\frac{1+\alpha}{2}} > 0. \end{aligned}$$

The negativity of α_1' is precisely the first condition of Theorem 4.4, which is essential for guaranteeing the decrease of $V(t)$ in the continuous stage.

Stage 2: Impulsive instants $(t = t_r)$**.**

At the discrete impulsive instant $t = t_r$, the hybrid impulsive controller executes a state jump correction for the synchronization error, and the parameter estimation $\zeta_i(t)$ is continuous (no impulsive jump) at impulsive instants. Thus the state jump rule for the synchronization error is

$$e_i(t_r) = (I + K) e_i(t_r^-), \tag{4.28}$$

where $e_i(t_r^-)$ denotes the left-hand limit of $e_i(t)$ at $t = t_r$. For the parameter estimation, we have $\zeta_i(t_r) = \zeta_i(t_r^-)$.

If we substitute the state jump rule into the Lyapunov function $V(t)$, the value of $V(t)$ at $t = t_r$ is

$$\begin{aligned} V(t_r) &= \frac{1}{2}\sum_{i=1}^{N} e_i^{\mathrm{T}}(t_r)Pe_i(t_r) + \frac{1}{2}\sum_{i=1}^{N}\left(\hat{\zeta} - \zeta_i(t_r)\right)^{\mathrm{T}}\left(\hat{\zeta} - \zeta_i(t_r)\right) \\ &= \frac{1}{2}\sum_{i=1}^{N} e_i^{\mathrm{T}}(t_r^-)(I+K)^T P(I+K)e_i(t_r^-) + \frac{1}{2}\sum_{i=1}^{N}\left(\hat{\zeta} - \zeta_i(t_r^-)\right)^{\mathrm{T}}\left(\hat{\zeta} - \zeta_i(t_r^-)\right). \end{aligned} \tag{4.29}$$

By the second condition of Theorem 4.4, i.e.,

$$(I+K)^T P(I+K) \le \nu^{\frac{2}{1-\alpha}} P,$$

the Lyapunov function at impulsive instants satisfies the following jump inequality:

$$V(t_r) \le \nu^{\frac{2}{1-\alpha}} V(t_r^-). \tag{4.30}$$

Stage 3: Combination of two stages and finite-time convergence.

Combining the continuous stage differential inequality (Eq (4.27)) and the impulsive stage jump inequality (Eq (4.30)), the closed-loop system's Lyapunov function satisfies the following impulsive nonlinear system:

$$\begin{cases} V(t) \le \alpha_1 V(t) - \alpha_2 V^q(t), & t \ne t_r, \\ V(t_r) \le \nu^{\frac{2}{1-\alpha}} V(t_r^-), & t = t_r, \end{cases} \tag{4.31}$$

where $q = \frac{1+\alpha}{2} \in (0,1)$ and the impulsive interval satisfies the third condition of Theorem 4.4

$$t_{r+1} - t_r \le \tau_{\max}.$$

The impulsive nonlinear system above is exactly the form of the system in Lemma 4.3 (take $\mu = \nu^{\frac{2}{1-\alpha}} \in (0,1)$). According to the conclusion of Lemma 4.3, the Lyapunov function $V(t)$ converges to zero in finite time T. Since $V(t)$ is a positive definite function of the synchronization error $e_i(t)$ and the parameter estimation error $\hat{\zeta} - \zeta_i(t)$, the convergence of $V(t) \to 0$ implies $\|e_i(t)\| \to 0$ for all $i = 1, 2, \cdots, N$ as $t \to T$.

Thus the CNN system achieves global finite-time synchronization, and the proof is completed. □

Remark 4.5. *Under the conditions of Theorem 4.4, the finite-time synchronization time T can be explicitly evaluated by substituting the parameters obtained in the proof of Theorem 4.4 into Lemma 4.3. Specifically, from Eqs (4.27) and (4.31), we have*

$$\alpha_1 = \frac{2}{p_{\min}}[\lambda_{\max}(\Gamma_s) + \epsilon + \nu_i\lambda_i^{\omega(t)} + \Lambda - \Upsilon - \kappa\xi\tau], \quad \alpha_2 = \frac{2\beta p_{\min}}{p_{\max}^{\frac{1+\alpha}{2}}}, \quad q = \frac{1+\alpha}{2}, \quad \mu = \nu^{\frac{2}{1-\alpha}}. \tag{4.32}$$

Substituting these four quantities into the expressions of Lemma 4.3, we have

$$\gamma = \mu e^{\alpha_1(1-q)\tau_{\max}}, \quad \theta = \frac{\alpha_2}{|\alpha_1|}, \quad \epsilon_0 = 1 - \left(\frac{\mu - 1}{\ln \mu}\right), \quad T_0 = \frac{2}{|\alpha_1|(1-q)}\ln(1-\epsilon_0), \tag{4.33}$$

the convergence time T is given explicitly, depending on the initial value $V(t_0)$, by one of the following three cases in Lemma 4.3:

Case 1: If $V(t_0) \leq (\epsilon_0\theta)^{\frac{1}{1-q}}$, *then* $T = T_0$ *;*
Case 2: If $V(t_0) > (\epsilon_0\theta)^{\frac{1}{1-q}}$ *and* $\gamma = 1$, *then*

$$r_0 = \left\lfloor \frac{V^{1-q}(t_0) - \epsilon_0\theta}{\theta(1-\mu)} \right\rfloor + 1, \quad T = r_0\tau_{\max} + T_0; \tag{4.34}$$

Case 3: If $(\epsilon_0\theta)^{\frac{1}{1-q}} < V(t_0) < \chi^*$ *and* $\gamma \neq 1$, *then*

$$r_0 = \left\lfloor \log_\gamma \frac{\left[\dfrac{\gamma-\mu}{1-\gamma} + \epsilon_0\right]\theta}{\dfrac{\gamma-\mu}{1-\gamma}\theta + V^{1-q}(t_0)} \right\rfloor + 1, \quad T = r_0\tau_{\max} + T_0. \tag{4.35}$$

Hence, T *is completely determined by the original controller and network parameters*

$$\{\Upsilon,\ \beta,\ \alpha,\ \kappa,\ \xi,\ \tau,\ K,\ \tau_{\max},\ \nu,\ P\},$$

together with the initial synchronization error (t_0)*, and can be numerically evaluated once these are specified—see the computation in Section 5.*

As direct consequences of Theorem 4.4, we present the following corollaries that address three practically important special cases: Fixed topology, identical neurons with no parameter uncertainty, and purely continuous control.

Corollary 4.6. *Consider Eq (2.2) under a fixed topology, i.e.,* $\omega(t) \equiv \omega_0$ *for some constant* $\omega_0 \in \{1, 2, \cdots, M\}$*, so that the Laplacian matrix* $Q^{\omega(t)} \equiv Q^{\omega_0}$ *is time-invariant. Under Assumptions 4.1 and 4.2 and Eq (3.1), if the following conditions hold:*

$$\begin{cases} \Upsilon > \lambda_{\max}(\Gamma_s) + \epsilon + \nu_i\,\lambda_i^{\omega_0} + \Lambda + \kappa\xi\tau, \\ (I+K)^{\mathrm{T}}\,P\,(I+K) \leq \nu^{\frac{2}{1-\alpha}}P, \\ t_{r+1} - t_r \leq \tau_{\max}, \end{cases} \tag{4.36}$$

where $\lambda_i^{\omega_0}$ *is the i-th eigenvalue of the fixed Laplacian matrix* Q^{ω_0}*, then the network achieves global finite-time synchronization with the convergence time* T *given by Lemma 4.3.*

Proof. Setting $\omega(t) \equiv \omega_0$ in Theorem 4.4 eliminates the time-varying dependence of $\lambda_i^{\omega(t)}$. The remainder of the proof follows directly from Theorem 4.4, with $\lambda_i^{\omega(t)}$ replaced by the constant $\lambda_i^{\omega_0}$. □

Remark 4.7. *Corollary 4.6 shows that Theorem 4.4 strictly generalizes classical finite-time synchronization results for fixed-topology CNNs. Under a fixed topology, the condition on* Υ *becomes time-invariant, which simplifies controller tuning in practice.*

Corollary 4.8. *Suppose that the parameters* $\zeta_i(t)$ *of all response neurons are exactly known and equal to the target parameter, i.e.,* $\zeta_i(t) \equiv \hat{\zeta}$ *for all* $i = 1, 2, \ldots, N$ *and all* $t \geq 0$*. Then Eq (3.5) is inactive, the parameter estimation error vanishes identically, and the Lyapunov function reduces to*

$$V(t) = \frac{1}{2}\sum_{i=1}^{N} e_i^{\mathrm{T}}(t)Pe_i(t). \tag{4.37}$$

Under Assumptions 4.1 and 4.2 and the hybrid impulsive controller (3.1), if the following conditions hold:

$$\begin{cases} \Upsilon > \lambda_{\max}(\Gamma_s) + \epsilon + \nu_i \lambda_i^{\omega(t)} + \Lambda, \\ (I+K)^{\mathrm{T}} P (I+K) \le \nu^{\frac{2}{1-\alpha}} P, \\ t_{r+1} - t_r \le \tau_{\max}, \end{cases} \tag{4.38}$$

then the network achieves global finite-time synchronization.

Proof. When $\zeta_i(t) \equiv \hat{\zeta}$, the second term of $V(t)$ in Eq (4.1) is zero. Consequently, the term $\kappa\xi\tau$ in the first condition of Theorem 4.4 vanishes, and the differential inequality (4.27) still holds with

$$\alpha_1 = \frac{2}{p_{\min}}[\lambda_{\max}(\Gamma_s) + \epsilon + \nu_i\lambda_i^{\omega(t)} + \Lambda - \Upsilon] < 0, \quad \alpha_2 = \frac{2\beta p_{\min}}{p_{\max}^{\frac{1+\alpha}{2}}} > 0.$$

Applying Lemma 4.3 completes the proof. □

Remark 4.9. *Corollary 4.8 demonstrates that, in the absence of parameter uncertainty, the proposed controller degenerates to a purely hybrid impulsive finite-time synchronization scheme without the need for parameter identification, thereby reducing online computational overhead.*

Corollary 4.10. *Consider the special case in which no impulsive corrections are applied, i.e., $K = 0$ (so that $I + K = I$) and the impulsive instants $\{t_r\}$ are absent. Under Assumptions 4.1 and 4.2 and the continuous part of controller (3.1), if*

$$\Upsilon > \lambda_{\max}(\Gamma_s) + \epsilon + \nu_i\lambda_i^{\omega(t)} + \Lambda + \kappa\xi\tau, \tag{4.39}$$

then the synchronization error satisfies $\lim_{t\to T} \|e_i(t)\| = 0$ for all $i = 1, 2, \cdots, N$, i.e., global finite-time synchronization is achieved by continuous feedback alone.

Proof. With $K = 0$, the second condition of Theorem 4.4 becomes $(I + K)^{\mathrm{T}}P(I + K) = P$, so the jump inequality (4.30) is trivially satisfied with equality $V(t_r) = V(t_r^-)$. The differential inequality (4.27) then holds globally on $[t_0, \infty)$, and finite-time convergence follows directly from the standard finite-time stability lemma applied to $\dot{V}(t) \le \alpha_1 V(t) - \alpha_2 V^q(t)$ with $\alpha_1 < 0$. □

Remark 4.11. *Corollary 4.10 establishes that the nonlinear power-law term $-\beta\,\mathrm{sign}(e_i)|e_i|^\alpha$ in the continuous controller alone is sufficient to guarantee finite-time synchronization, provided that the linear gain Υ satisfies Condition (4.39). This result is practically significant when impulsive actuation is unavailable or undesirable.*

5. Numerical simulations

In this section, a numerical example is provided to demonstrate the validity of the synchronization criteria. The uncertain network is considered under a switching topology consisting of N neurons.

The coupled FitzHugh-Nagumo (FHN) network (Eq (2.2)) and the target system (Eq (2.3)) were integrated using the forward Euler method with a fixed time step of $h = 0.01$ s. The total simulation duration was $T_{\text{sim}} = 10$ s (1000 time steps). The network consists of $N = 15$ nodes and $M = 5$

distinct topology modes. The five Laplacian matrices $\{Q^{(\omega)}\}_{\omega=1}^{5}$ were randomly generated at the start of each simulation run via the topology decrease function: For each mode, an undirected adjacency matrix was constructed by randomly assigning each node exactly $d = 6$ neighbors (chosen uniformly without replacement from the remaining $N - 1$ nodes), and the Laplacian was then derived from this adjacency matrix in the standard way ($q_{ii}^{(\omega)} = -\sum_{j\neq i} q_{ij}^{(\omega)}$, $q_{ij}^{(\omega)} \in \{0, 1\}$ for $i \neq j$). The topology switching signal $\omega(t)$ was generated as follows: At each time step n, an independent uniform random variable $r_n \sim \mathcal{U}(0, 1)$ was drawn; if $r_n > 0.95$, the topology switched to a new mode selected uniformly at random from $\{1, 2, 3, 4, 5\}$; otherwise, the topology remained unchanged. This yields an expected dwell time of approximately $1/(0.05 \times h^{-1}) = 0.2$ s per mode at each potential switch. The x-direction and y-direction coupling strengths were set to $\upsilon_x = 0.5$ and $\upsilon_y = 0.3$, respectively. The Lyapunov weight matrix was chosen as $P = I_2$ (the 2×2 identity matrix), giving $p_{\min} = p_{\max} = 1$.

The initial conditions were specified as follows. For the i-th response node ($i = 1, 2, \cdots, 15$), we have the membrane potential $x_i(0) = 0.1 - 0.05i$ and the recovery variable $y_i(0) = 0.1 + 0.05i$, yielding

$$x_i(0) \in [-0.65, 0.05] \quad \text{and} \quad y_i(0) \in [0.15, 0.85],$$

across the 15 nodes. The initial parameter estimate for each node was $\hat{c}_i(0) = 0.1 + 0.02i$, giving $\hat{c}_i(0) \in [0.12, 0.40]$ and an initial estimation error of $|c - \hat{c}_i(0)| \in [0.30, 0.58]$ relative to the true value $c = 0.1$. The target (drive) system was initialized at $x_{\text{target}}(0) = 0.1$ and $y_{\text{target}}(0) = 0.1$. The external stimulation applied to both the response and target systems is $I_{\text{ext}}(t) = A_1 \sin(\omega_1 t) + A_2 \cos(\omega_2 t)$ with $A_1 = 1$, $\omega_1 = 1$, $A_2 = 0.1$, and $\omega_2 = 1$.

A simplified FHN neuronal model is described as follows [35]:

$$\begin{cases} \dfrac{dx}{dt} = x(1-\delta) - \dfrac{1}{3}x^3 - y + \Xi, \\ \dfrac{dy}{dt} = c(x - by + a), \end{cases} \tag{5.1}$$

where x represents the membrane potential, and y denotes the recovery variable. The parameters a, b, c, and δ are used to regulate the neuronal firing patterns. The external stimulus Ξ is defined as

$$\Xi = \Lambda_1 \sin(\omega_1 t) + \Lambda_2 \cos(\omega_2 t). \tag{5.2}$$

The evolution of Lyapunov exponents for the FHN neuronal system with varying driving frequencies ω_1 and ω_2 is illustrated in Figure 2. The FHN neuronal system exhibits rich dynamic behaviors in the parameter space of dual-frequency driving. When $\lambda_1 < 0$ and $\lambda_2 < 0$, the neuron remains in a stable state; when $\lambda_1 \approx 0$ and $\lambda_2 < 0$, it enters a quasiperiodic state; and when $\lambda_1 > 0$, the neuron displays chaotic dynamics. As shown in Figure 2a, the largest Lyapunov exponent λ_1 is negative over most of the parameter space, with isolated "peaks" of positive values (in red) appearing only in localized regions, indicating that chaotic states are sparsely and discretely distributed. In Figure 2b, λ_2 remains negative throughout and takes on even smaller (more negative) values, reflecting pronounced dissipative characteristics. In Figure 2c, the boundary where $\lambda_1 = 0$ (black curve) clearly separates stable and chaotic regions, revealing a complex fractal-like structure, particularly within the interval $\omega_1 \in [0.8, 1.5]$, where multiple "island-like" unstable zones emerge. Figure 2d shows that the region where λ_2 is negative dominates the parameter space, with smooth and gradual transitions. Overall, 95.78% of the sampled points correspond to stable dynamics, demonstrating the system's strong robustness to dual-frequency stimulation, while chaotic behavior occurs only near specific frequency ratios, accounting for just 3.11% of the cases. This provides a dynamic basis for frequency-selective encoding in neurons.

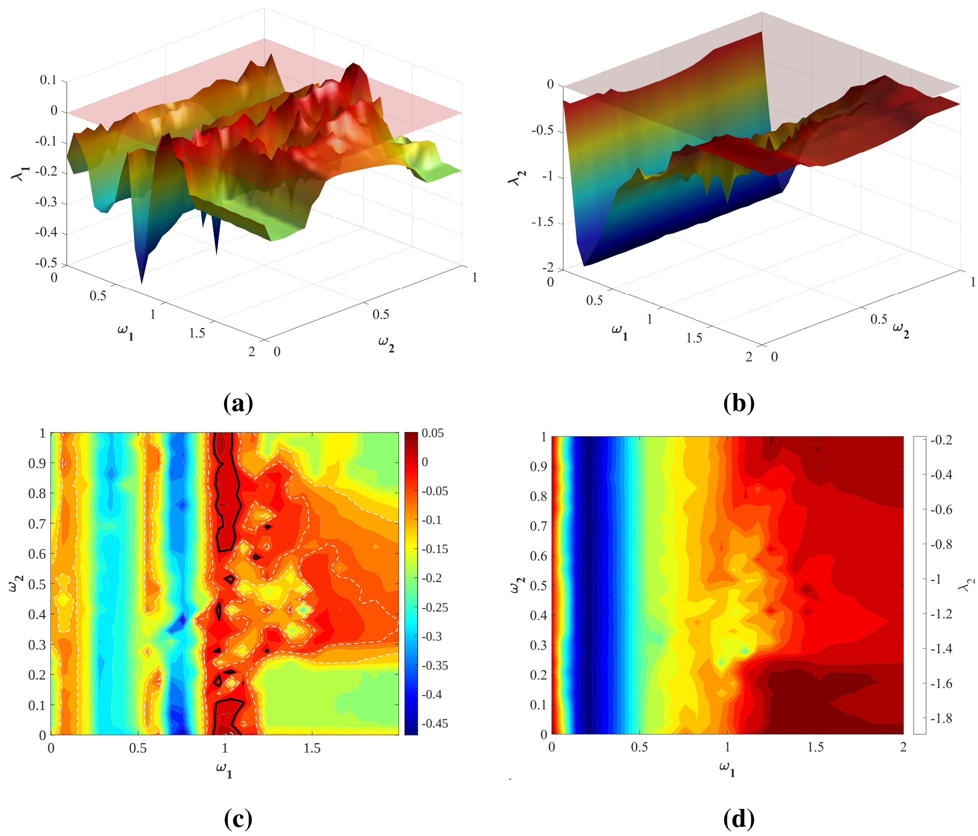

Figure 2. Evolution of Lyapunov exponents with the parameters ω_1 and ω_2 ($a = 0.7, b = 0.8, c = 0.1$). (a)–(b) Surface plots of λ_1 and λ_2, respectively. (c)–(d) Contour plots of λ_1 and λ_2, respectively.

Figure 3 illustrates how the FHN neuron exhibits distinct dynamic regimes under different driving frequencies. At a lower frequency, Figure 3a displays periodic burst-silence alternations, with approximately 10–12 bursts occurring over 2000 time units—a classic signature of neuronal bursting. The corresponding phase portrait in Figure 3d reveals a complex attractor composed of multiple loops, reflecting recurrent transitions between active firing and quiescent phases. In contrast, at an intermediate frequency, Figure 3b shows regular high-frequency oscillations with a consistent amplitude, characteristic of tonic spiking. This behavior is mirrored in Figure 3e, where the trajectory converges to a smooth, stable limit cycle, indicating sustained periodic single-spike firing without bursting modulation. At a higher driving frequency, the system enters a chaotic regime: Figure 3c exhibits irregular, aperiodic oscillations with pronounced amplitude modulation, while Figure 3f shows densely overlapping trajectories forming a chaotic attractor-consistent with the positive largest Lyapunov exponent identified in the prior parameter scan.

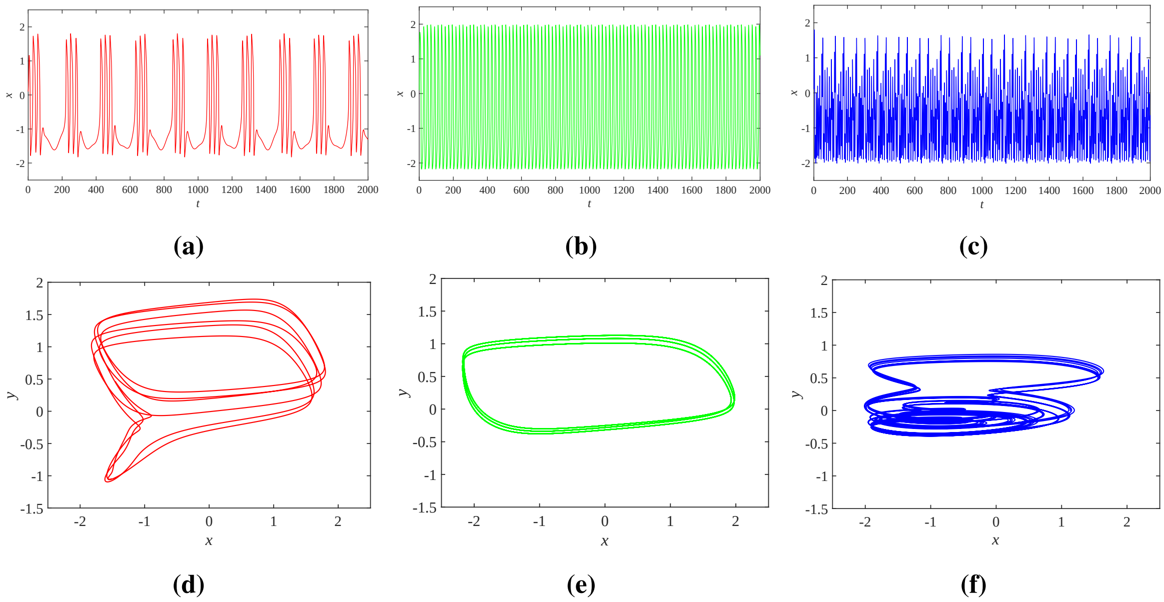

Figure 3. Firing patterns of the single FHN neuron ($a = 0.7$, $b = 0.8$, $c = 0.1$, $\xi = 0.15$, $\Lambda_1 = 1$, $\Lambda_2 = 0.1$, and $\omega_2 = 0.1$). (a)–(c) Membrane potential x at low, intermediate, and high driving frequencies, respectively. (d)–(f) Phase portraits corresponding to (a)–(c), respectively.

Together, this frequency-dependent transition from bursting to tonic spiking and finally to chaos demonstrates how external periodic forcing can fundamentally reshape neuronal excitability. These findings offer valuable insights into the mechanisms of neural encoding under oscillatory inputs, highlighting the role of drive frequency in modulating dynamic complexity.

Consider a CNN consisting of $N = 15$ neurons with the parameters $a = 0.7$, $b = 0.8$, $\delta = 0.15$, $A_1 = 1$, $A_2 = 0.1$, $\omega_1 = 1$, and $\omega_2 = 1$, where the parameter c is taken as the parameter to be identified, with its value set to 0.1 in the target system. As shown in Figure 4, it is assumed that the network topology has five types, and the network topology switches between $\omega(t) = 1$, $\omega(t) = 2$, $\omega(t) = 3$, $\omega(t) = 4$, and $\omega(t) = 5$. The five distinct network topologies reflect the diversity and uncertainty of network structures. The random switching among these topologies simulates dynamic structural changes in practical applications, representing a critical design for verifying the robustness of control strategies. As shown in Figure 5, the random switching process of network topologies along the time axis via the switching signal plot. The five topology modes exhibit irregular transitions both before and after controller activation, realistically reflecting the time-varying nature of topologies in actual network environments.

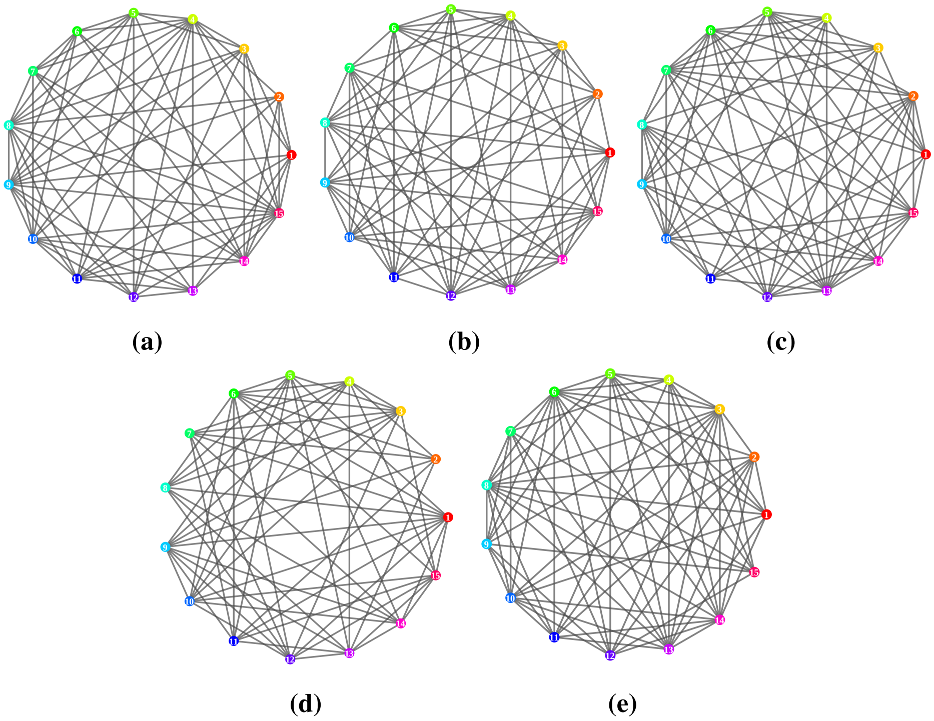

Figure 4. Network topologies for $N = 15$.

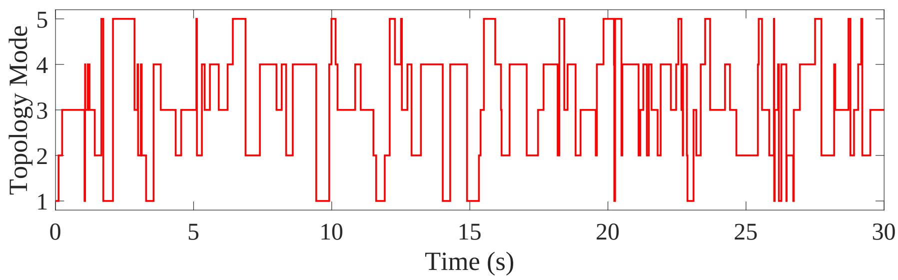

Figure 5. Switching signal in the numerical example.

The control parameters are set as $\Upsilon = 3.0$, $\alpha = 0.7$, $\beta = 4.0$, $\tau_{\max} = 5.0$ s, $\upsilon = 0.8$, and

$$K = \left(0.8^{\frac{1}{1-0.7}} - 1\right) I \approx -0.587\, I.$$

As shown in Figure 6, the temporal evolution of synchronization errors is presented. Prior to controller activation, the synchronization errors exhibit relatively large initial values, with different curves representing distinct dynamic behaviors across the network nodes. Following controller activation, all synchronization errors undergo rapid decay. The curves demonstrate a swift convergence process, with all errors approaching zero within approximately 0.5 seconds. This rapid convergence indicates that the proposed control strategy effectively synchronizes the system's states in a short time interval. The convergence trajectories are smooth and monotonic, showing no oscillations or overshooting phenomena, validating the stability and effectiveness of the control method. The different colored curves likely represent various network nodes or state variables, all exhibiting similar convergence patterns despite potentially different initial conditions, demonstrating the robustness of the control approach in achieving uniform synchronization across the entire network under uncertain conditions and randomly switching topologies.

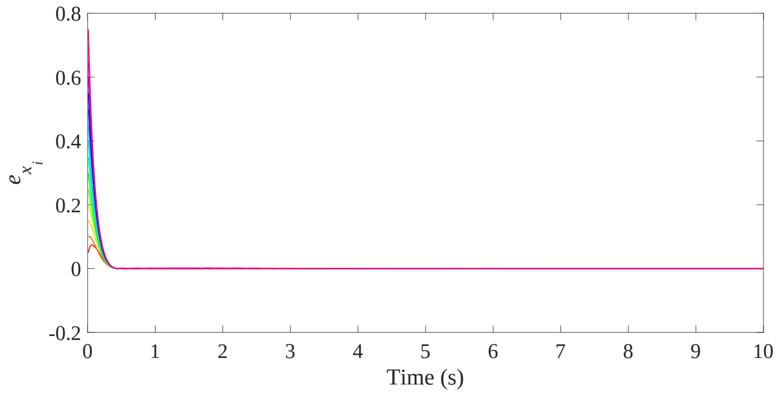

Figure 6. Evolution of errors $e_{x_i}(t)$ $(i = 1, 2, \cdots, 15)$.

The controller parameters were set as follows: Linear gain $\gamma = 3.0$, nonlinear gain $\beta = 4.0$, power-law exponent $\alpha = 0.7$, and maximum inter-impulse interval $\tau_{\max} = 5.0$ s (corresponding to 500 time steps). The impulsive contraction coefficient was $\nu = 0.8$, and the scalar impulsive gain was

$$K_{\text{scalar}} = \nu^{1/(1-\alpha)} - 1 = 0.8^{1/0.3} - 1 \approx -0.5874,$$

so the impulsive gain matrix is

$$K = K_{\text{scalar}} \cdot I_2 \approx -0.5874 I_2.$$

One may verify that

$$(I + K)^{\mathrm{T}} P (I + K) = (1 + K_{\text{scalar}})^2 I_2 = 0.8^{2/0.3} I_2 \approx 0.1706 I_2,$$

while

$$\nu^{2(1-\alpha)} P = 0.8^{0.6} I_2 \approx 0.8706 I_2,$$

so the second condition of Theorem 4.4 is satisfied with a margin. Impulse instants $\{t_r\}$ were generated deterministically: The first impulse was applied at $t_1 = \tau_{\max} = 5.0$ s (Step 500), and each subsequent impulse at $t_{r+1} = t_r + \tau_{\max}$, giving exactly 2 impulses within $T_{\text{sim}} = 10$ s. The Newton iterative parameter identification parameters were as follows: Adaptation rate $\kappa = 1.0$, synchronization error weight $\tau = 0.1$, and parameter error weight $\xi = 0.5$. The parameter update was frozen when $|\hat{c}_i - c| \leq 10^{-6}$ to prevent numerical issues near convergence. Convergence of the synchronization error was declared when the ℓ^2 norm of the total error vector

$$\|e(t)\| = \sqrt{\sum_{i=1}^{N} \left(|e_{x,i}|^2 + |e_{y,i}|^2\right)}$$

fell below the threshold $\delta_s = 0.1$.

As shown in Figure 7, the temporal evolution of synchronization errors for the y component exhibits dynamic characteristics highly consistent with those observed in Figure 6. The synchronization errors display relatively large initial values with diverse starting conditions across different network nodes. Upon activation of the control strategy, all error trajectories undergo rapid exponential convergence toward zero. The convergence process is completed within approximately 0.5 seconds, mirroring the convergence speed observed in the x component. The error trajectories are smooth and monotonic without oscillations, demonstrating stable and efficient control performance. Notably, the convergence patterns of the y component closely resemble those of the x component, indicating that the proposed control strategy achieves uniform effectiveness across different state variables. This consistency reflects the controller's capability to handle the strong coupling among state variables in the three-dimensional chaotic system. The synchronized convergence behavior across multiple state dimensions validates the robustness and reliability of the hybrid impulsive control method in managing multi-dimensional dynamic systems under uncertain conditions and randomly switching topologies, providing strong evidence for coordinated multi-state synchronization in complex networks.

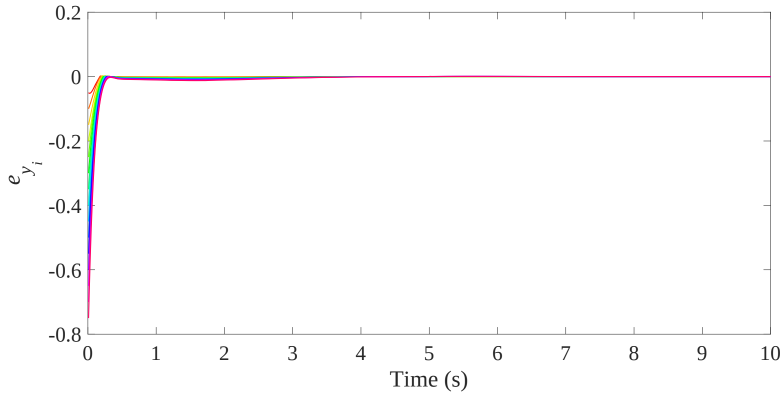

Figure 7. Evolution of errors $e_{y_i}(t)$ $(i = 1, 2, \cdots, 15)$.

As shown in Figure 8, the uncertain parameters c_i of the 15 network nodes converge to the target value of 0.1 (indicated by the horizontal dashed line) from their arbitrary initial values. Starting from various initial conditions ranging approximately from 0.1 to 0.4, all parameter estimation trajectories exhibit smooth exponential decay and converge to the true parameter value within approximately 10 seconds. The convergence curves are monotonic without oscillations, demonstrating stable and robust identification performance. This result validates the effectiveness of the Newton iteration-based parameter identification mechanism, which leverages second-order derivative information to achieve rapid convergence rates superior to traditional gradient descent methods. The different colored curves represent individual network nodes, and despite their varying initial conditions, all parameters successfully converge to the same target value, highlighting the algorithm's consistency and reliability. Notably, the parameter identification process operates concurrently with network synchronization and is not constrained by the synchronization dynamics, enabling the system to accurately estimate unknown parameters while simultaneously achieving state synchronization across the network. This demonstrates the dual capability of the proposed control strategy in handling both synchronization and parameter identification tasks in uncertain complex networks.

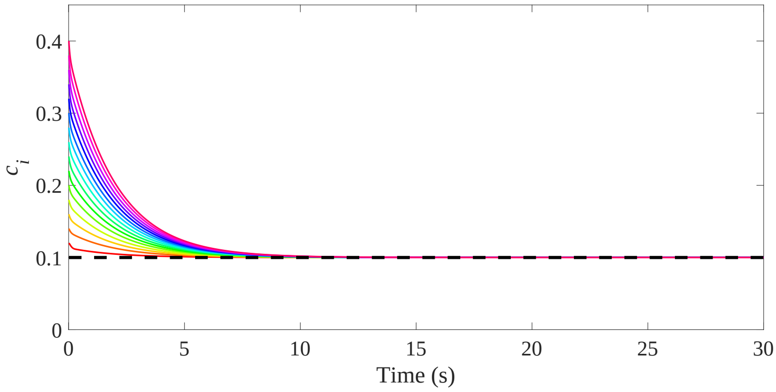

Figure 8. Identification processes of the parameter c_i.

Figure 9 illustrates the time evolution of the control input under Eq (3.1). As shown in Figure 9a, the control input norms $\|U_i(t)\|$ for all nodes exhibit a sharp initial transient, decaying rapidly from large values to near zero within approximately 1 second, which reflects the fast suppression of the initially large synchronization errors by the continuous control term. Figure 9b presents the average control input norm on a logarithmic scale, revealing a clear dip immediately followed by a discrete jump at the impulsive instant $t = 5$ s (dashed line), corresponding to the discrete state correction $Ke_i(t_r^-)$ in Eq (3.1). After the impulsive correction, the control input decays further and stabilizes at a small bounded magnitude, without exhibiting chattering or divergence. These results confirm that the proposed hybrid controller achieves finite-time synchronization while maintaining bounded and practically implementable control effort.

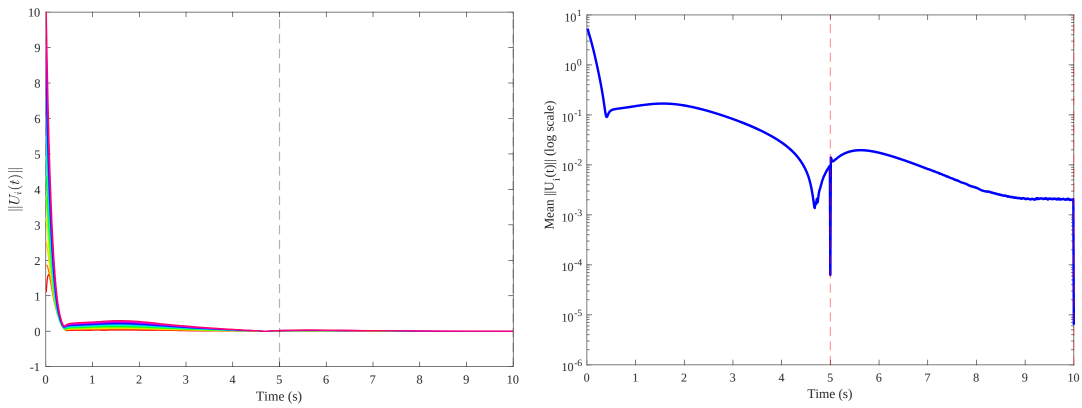

(a) **(b)**

Figure 9. Time responses of the control input $U_i(t)$ under the proposed hybrid impulsive controller. (a) Control input norm $\|U_i(t)\|$ for all $N = 15$ network nodes. (b) Average control input norm across the network (logarithmic scale), with the dashed line indicating the impulsive instant $t = 5$ s.

To further examine the scalability of the proposed hybrid impulsive control scheme, we extend the simulation to a large-scale coupled FHN network consisting of $N = 100$ neurons with $M = 5$ switching topology modes. All system and controller parameters are kept identical to those in the $N = 15$ case, so that the scalability of the method rather than parameter retuning is demonstrated.

The key theoretical conditions in Theorem 4.4 are network-size independent in the following sense. The first condition, namely

$$\Upsilon > \Gamma + \epsilon + v_i \lambda_i^{\omega(t)} + \Lambda + \kappa\xi\tau, \tag{5.3}$$

involves the i-th eigenvalue $\lambda_i^{\omega(t)}$ of the Laplacian matrix $Q^{\omega(t)}$. Although the spectrum of $Q^{\omega(t)}$ depends on the network's topology, the maximum eigenvalue $\lambda_{\max}^{\omega(t)}$ is bounded above by the maximum node degree $d_{\max}$ (a graph-theoretic property independent of N for sparse graphs). For the random sparse topologies used here, $d_{\max}$ remains bounded as N grows, so the condition in (5.3) can be satisfied with the same Υ regardless of the network's size. The second condition $(I+K)^{\mathrm{T}}P(I+K) \le \nu^{2/(1-\alpha)}P$ and the third condition $t_{r+1} - t_r \le \tau_{\max}$ are likewise independent of N.

The simulation results for $N = 100$ are presented in Figure 10. Figure 10a shows the evolution of the total synchronization error norm

$$\|e(t)\| = (\sum_{i=1}^{100} \|e_i(t)\|^2)^{1/2}$$

on a logarithmic scale. The error converges to zero within a finite time, consistent with Theorem 4.4. Figure 10b displays the Lyapunov function $V(t)$, which decreases monotonically between impulse instants and exhibits discrete jumps at $t = t_r$: the overall trend confirms the impulsive differential inequality (4.31). Figure 10c illustrates the parameter identification process: All 100 nodal estimates $c_i(t)$ converge to the true value $c = 0.1$, validating the Eq (3.5) at scale.

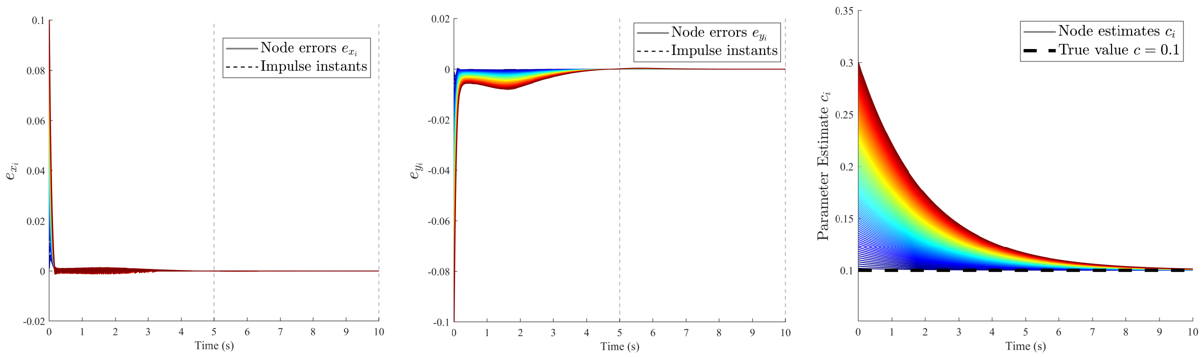

(a) **(b)** **(c)**

Figure 10. Synchronization errors and parameter identification for the coupled FHN network with $N = 100$ neurons under the hybrid impulsive controller. (a) Synchronization error $e_{xi}(t)$ $(i = 1, 2, \cdots, 100)$. (b) Synchronization error $e_{yi}(t)$. (c) Parameter identification process of c_i.

The results in Figure 10 demonstrate that the proposed method scales gracefully to large networks. Both the convergence time and the final synchronization/parameter identification errors remain comparable between $N = 15$ and $N = 100$, confirming that the theoretical conditions of Theorem 4.4 are sufficient for arbitrarily large (sparse) networks without requiring retuning of the controller parameters.

6. Performance analysis

Figure 11 shows the panoramic view of the synchronization convergence time against control gains. Overall, the system achieves synchronization over the vast majority of the parameter space, with only a small nonconvergent gray area observed in the lower left region. This nonconvergent region is bounded by a diagonal boundary that extends from approximately ($\Upsilon \approx 1$, $\beta \approx 4$) to ($\Upsilon \approx 6$, $\beta \approx 1$), occupying less than 15% of the total parameter space. This indicates that the proposed hybrid control strategy possesses wide applicability and strong robustness. The convergence time exhibits a clear gradient distribution pattern along the diagonal direction. The region near the nonconvergence boundary, shown in yellow-green, corresponds to a relatively longer convergence time of approximately 6–8 seconds. The central region appears in cyan, indicating a convergence time of approximately 2–4 seconds. The upper right region is predominantly dark blue, where the convergence time is further reduced to approximately 0–2 seconds. This pattern reveals a positive correlation between the magnitudes of the control gains and the convergence speed: Stronger linear and nonlinear control actions suppress synchronization errors more rapidly. It is particularly noteworthy that an "efficient convergence zone" is formed in the region where $\Upsilon > 4$ and $\beta > 4$, within which the convergence time remains below 2 seconds. Statistical data show that over 85% of the parameter combinations achieve convergence. The fastest convergence time is approximately 0–1 second, the slowest converged point is around 8–10 seconds (located near the nonconvergence boundary), and the average convergence time lies between 2 and 4 seconds.

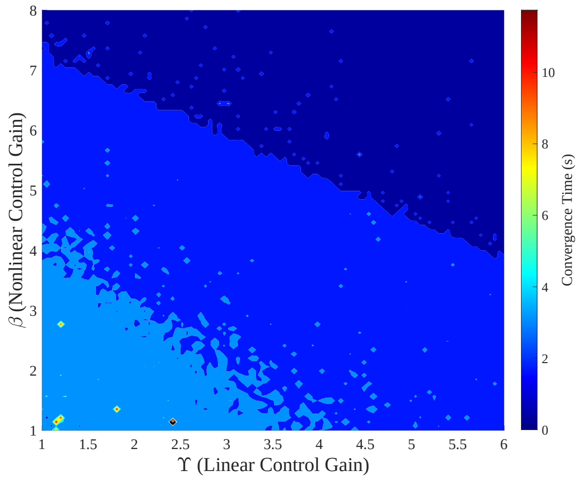

Figure 11. Evolution of synchronization time with β and Υ ($N = 15$, $\omega(t) \in \{1, 2, \cdots, 5\}$; gray area: failure to converge).

Figure 12 reveals the physical significance of the weighting parameters: τ, as the error weight, needs to be sufficiently large to provide a strong driving force, whereas ξ, as the parameter weight, should be kept relatively small to avoid excessive oscillation in parameter estimation. The convergence region spans nearly the entire (τ, ξ) parameter space, with non-convergent points indicated solely by the dark diamond markers with black outlines. These non-convergent points are predominantly concentrated in the lower right region, and their irregular distribution reflects the complex nonlinear characteristics of the system's dynamics. The convergence time exhibits a clear gradient pattern: The lower portion (low ξ region) is displayed dark blue, indicating fast convergence; the upper portion appears in cyan, corresponding to moderate convergence times; while the transition zone shows yellow to red colors, representing slower convergence.

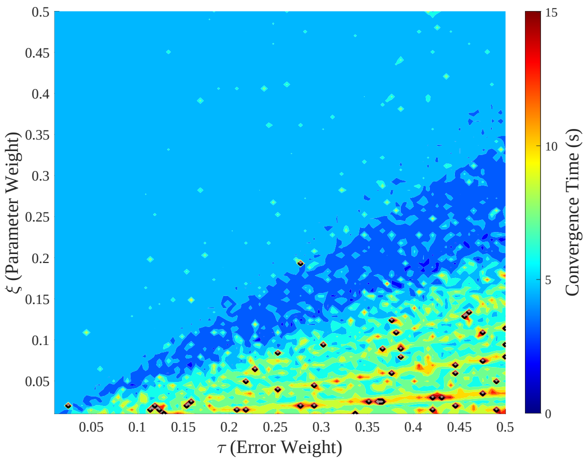

Figure 12. Evolution of parameter identification with τ and ξ ($N = 15$, $\omega(t) \in \{1, 2, \cdots, 5\}$; gray area: failure to converge).

In summary, the hybrid impulsive control strategy demonstrates excellent global convergence performance: As shown in Figure 11, over 85% of the sampled (Υ, β) combinations achieve synchronization convergence, and as shown in Figure 12, a comparably high proportion of the (τ, ξ) parameter space achieves successful parameter identification convergence. The primary distinction lies in their parametric sensitivity concerning the convergence speed: Synchronization control responds sensitively to the gain parameters, where increasing the control gains significantly accelerates convergence. In contrast, parameter identification is more demanding on the weight configuration, requiring a delicate balance between τ and ξ; specifically, τ should be moderately large, while ξ must remain small, as illustrated by the fast convergence region confined to the lower left of the heatmap.

7. Robustness analysis

To evaluate the robustness of the proposed hybrid impulsive controller, two independent sources of uncertainty are introduced into the simulation, in accordance with the following.

(1) **External disturbance**: A zero-mean additive stochastic (white noise) perturbation directly injected into the state derivatives $\dot{x}_i(t)$ and $\dot{y}_i(t)$ of each response node, representing exogenous environmental or measurement-type noise acting on the neuronal dynamics. Three intensity levels are tested—low (0.01), medium (0.05), and high (0.10)—corresponding to the noise amplitude scale.

(2) **Parametric uncertainty**: The standard deviation of a random, node-to-node Gaussian mismatch applied to the nominal FHN parameters $a = 0.7$ and $b = 0.8$ of each response node relative to the target system. This models structural/parametric heterogeneity among neurons rather than random noise, i.e., each node's true parameters (a, b) deviate from the nominal values by a fixed random offset drawn with standard deviation (0.02/0.05/0.10 for low/medium/high), held constant throughout the simulation.

Figure 13 presents a comparison of the logarithmic curves of the synchronization error norm $\|e(t)\|$

under different disturbance/uncertainty scenarios, where "disturbance" denotes additive stochastic noise injected into the node dynamics and "uncertainty" denotes a fixed random mismatch between each node's FHN parameters (a, b) and the nominal target values, where "std" denotes the standard deviation of parameter uncertainty. It can be observed that the curves for the pure parameter uncertainty scenarios (low/medium/high) almost completely overlap with the baseline curve, indicating that the proposed controller exhibits strong robustness against parametric uncertainty, with the error eventually converging to below the order of 10^{-4}. In contrast, the three curves with external disturbances (low/medium/high intensity) all tend to a nonzero noise floor after the initial fast convergence, and the floor level increases with the disturbance's intensity, which is consistent with the theoretical expectation that random disturbances cannot be completely suppressed by a finite-time controller. The steady-state error in the combined severe scenario is slightly higher than that in the pure uncertainty scenario, but remains significantly lower than that in the pure disturbance scenario, demonstrating that the controller maintains effective error suppression capability even under combined uncertainties.

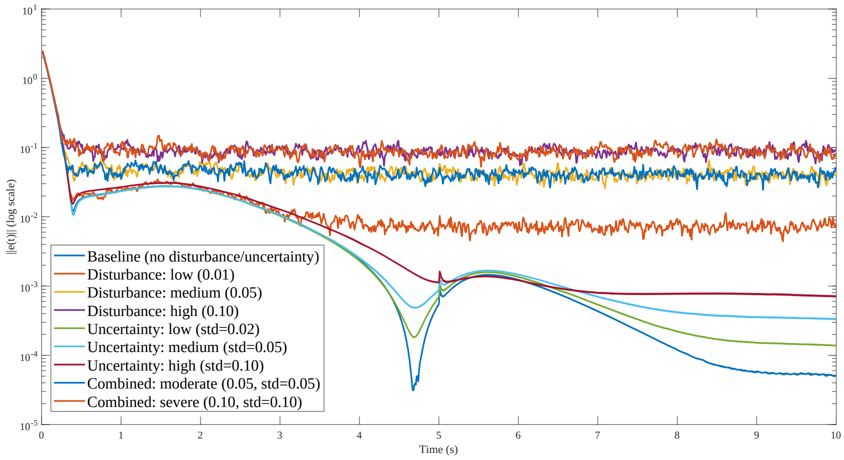

Figure 13. Synchronization error norm under varying disturbance and parametric uncertainty.

As shown in Figure 14, the logarithmic curves of the average parameter identification error $|c_i - c|$ over time are presented for each scenario, where the identified quantity is the coupling-related parameter c and the disturbance/uncertainty definitions are identical to those described above. In scenarios without external disturbances (baseline, pure uncertainty, and combined scenarios), the identification error exhibits an approximately exponential decay trend, dropping to around the order of 10^{-3} within 10 seconds, which verifies the fast convergence property of the Newton iteration-based adaptive law. In contrast, in scenarios with external disturbances, the identification error exhibits noticeable jagged fluctuations during the convergence process, and for higher disturbance intensities (medium and high), it tends to settle at a relatively high plateau of approximately 2×10^{-2} around $t \approx 6$–10 s. This indicates that persistent random disturbances are coupled into the parameter update law through the synchronization error term, thereby limiting further improvement in parameter identification accuracy.

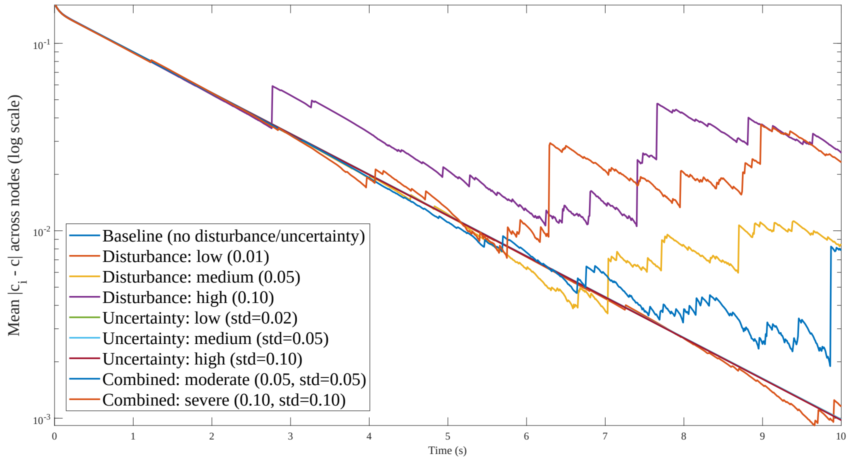

Figure 14. Parameter identification error across varying disturbance and parametric uncertainty.

8. Comparative analysis

This section presents a comparative analysis between the parameter identification method based on Newton iteration proposed in this paper and three classical parameter identification methods: Gradient descent [39], adaptive law [40], and sliding mode adaptive [41]. The descriptions of these three benchmark methods are provided as follows.

The gradient descent method updates the parameter estimate by following the negative gradient of the error function. For the FHN neuronal system with the uncertain parameter a, the update law is

$$\frac{d\hat{a}_i}{dt} = -\gamma_g \nabla_{\hat{a}_i} J(e_i, a_i), \tag{8.1}$$

where $\hat{a}_i$ is estimated value of parameter a by node i, γ_g demonstrates the learning rate, $J(e_i, \hat{a}_i)$ is the cost function, typically chosen as

$$J = \frac{1}{2} e_i^T e_i,$$

therefore, the gradient descent update law becomes

$$\frac{d\hat{a}_i}{dt} = \gamma_g e_{x_i}(y_i - x_i). \tag{8.2}$$

The adaptive law method uses online parameter adjustment based on the Lyapunov stability theory. The update law is designed to ensure negative definiteness of the Lyapunov derivative

$$\frac{d\hat{a}_i}{dt} = \eta e_{x_i} (y_i - x_i) - \sigma (a_i - a_0), \tag{8.3}$$

where η represents adaptive gain, σ demonstrates the parameter decay term, and a_0 is the prior parameter estimate.

The sliding mode adaptive method combines the robustness of sliding mode control with parameter adaptation. The method defines a sliding surface and uses a discontinuous control law to drive the system onto the surface. The update law consists of sliding mode term and gradient term as follows:

$$\frac{d\hat{a}_i}{dt} = \rho\,|s_i| \cdot \mathrm{sign}\,(a - a_i) + k_s s_i\,(y_i - x_i)\,, \tag{8.4}$$

where s_i is the sliding surface, ρ represents the adaptation rate, and k_s demonstrates the sliding mode gain. To reduce chattering, the sign function sign$(\cdot)$ is replaced by a saturation function sat$(*, *)$ as follows:

$$\mathrm{sat}(s_i,\,\phi) = \begin{cases} \mathrm{sign}(s_i), & |s_i| > \phi, \\ \dfrac{s_i}{\phi}, & |s_i| \le \phi, \end{cases} \tag{8.5}$$

where ϕ is the boundary layer's thickness.

To enable a performance comparison between the proposed parameter identification method and the three aforementioned methods, E_p and $||e||$ are defined as follows:

$$E_p(t) = \frac{1}{N}\sum_{i=1}^{N} |c_i(t) - c|\,, \tag{8.6}$$

where E_p demonstrates the average parameter error $|\hat{c}_i(t) - c|$.

$$||e|| = \frac{1}{N}\sum_{i=1}^{N} \sqrt{e_{x_i}^2 + e_{y_i}^2}, \tag{8.7}$$

where $||e||$ demonstrates the average synchronization error.

Under conditions ensuring complete fairness, we compare the aforementioned three methods with the proposed method in terms of the synchronization speed and parameter identification speed, with the following parameter assignments. The parameters for the proposed method are $\kappa = 1.0$, $\tau = 0.1$, and $\xi = 0.5$; for the gradient descent method, $\gamma_g = 0.8$; for the adaptive law method, $\eta = 0.5$ and $\sigma = 0.1$; and for the sliding mode adaptive method, $k_s = 0.6$, $\rho = 0.5$, and $\phi = 0.8$.

As shown in Figure 15, the mean synchronization error norm is plotted against time for four different methods. Newton iteration demonstrates the fastest convergence, with the synchronization error rapidly approaching zero. Gradient descent exhibits the slowest convergence, characterized by a gradual error decay. Both the adaptive law and sliding mode adaptive methods show intermediate convergence speeds. Notably, the sliding mode adaptive approach exhibits significant initial oscillations with the number of error peaks reaching approximately 30, but achieves stable performance after around 15 seconds. All four methods eventually converge to zero synchronization error by the end of the 50-second simulation period. This validates the theoretical convergence speed ranking: Newton iteration is the fastest, followed by the sliding mode adaptive and adaptive law methods with comparable performance, while gradient descent is the slowest.

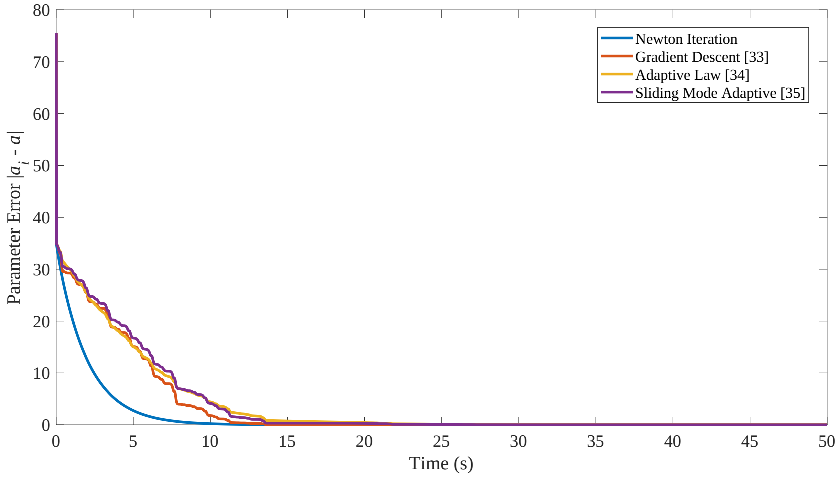

Figure 15. Comparison of synchronization error ($N = 150$ and $\omega(t) \in \{1, 2, \cdots, 5\}$, $\gamma_g = -0.8$, $\eta = 0.3$, $\sigma = 0.1$, $k_s = 0.5$, $\phi = 0.8$, and $\rho = 0.5$).

As shown in Figure 16, the mean parameter error is plotted against time for the four different methods. Newton iteration demonstrates superior parameter convergence, with the error decreasing most rapidly and approaching zero within approximately 5 seconds. Gradient descent and adaptive law exhibit similar convergence rates, both reaching zero error around 10 to 12 seconds. The sliding mode adaptive method displays characteristic step-like chattering behavior throughout the convergence process, but ultimately achieves similar convergence time to gradient descent and adaptive law. All four methods successfully converge to zero parameter error by the end of the simulation. This indicates that while Newton iteration offers the fastest parameter identification, the sliding mode adaptive method maintains acceptable parameter identification capability while providing additional robustness through its inherent chattering mechanism.

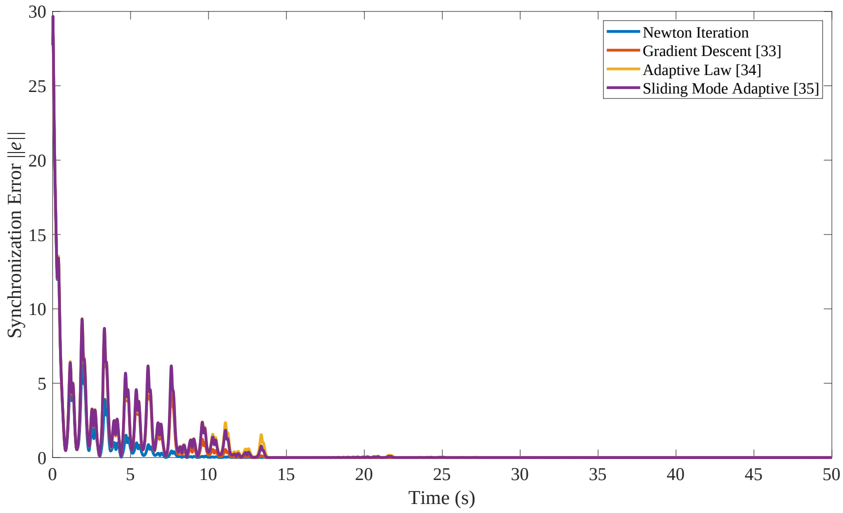

Figure 16. Comparison of parameter identification error ($N = 150$, $\omega(t) \in \{1, 2, \cdots, 5\}$, $\gamma_g = -0.8$, $\eta = 0.3$, $\sigma = 0.1$, $k_s = 0.5$, $\phi = 0.8$, and $\rho = 0.5$).

As shown in Figure 17, the performance comparison of the four methods is presented across four metrics. Newton iteration outperforms the other methods in all metrics, achieving the lowest final parameter error, the lowest final synchronization error, and the shortest convergence times for both parameter and synchronization. The adaptive law demonstrates the second-best performance in terms of final parameter error, while the gradient descent and sliding mode adaptive methods show comparable final synchronization errors. Regarding the convergence speed, gradient descent and adaptive law exhibit a similar parameter convergence times, whereas the sliding mode adaptive method requires the longest parameter convergence time due to its inherent chattering behavior. For the synchronization convergence time, gradient descent, adaptive law, and sliding mode adaptive methods perform similarly. Overall, Newton iteration is the optimal choice for scenarios requiring high accuracy and fast convergence, while the adaptive law offers a balanced trade-off between accuracy and computational complexity.

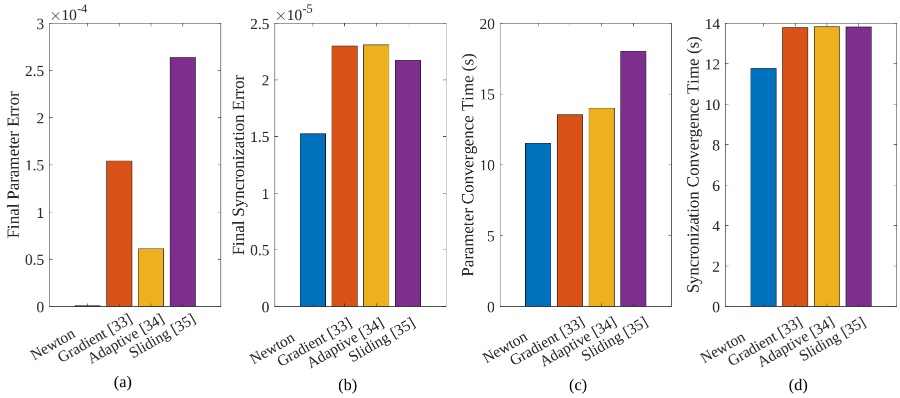

Figure 17. Comparison of performance metrics: (a) identification error, (b) synchronization error, (c) parameter convergence time, and (d) synchronization convergence time ($N = 150$, $\omega(t) \in \{1, 2, \cdots, 5\}$).

Based on the simulation results presented in Figures 15–17 and Table 1, a comprehensive comparison of the four parameter identification methods is conducted. The proposed method demonstrates the best overall performance, achieving the shortest identification time of 11.52 seconds, the fastest synchronization time of 11.77 seconds, and the highest accuracy, with a parameter error of 9.9858×10^{-7} and a synchronization error of 1.5247×10^{-5}. The convergence curves confirm that proposed method reaches a steady state the most rapidly without oscillations. Gradient descent and the adaptive law exhibit comparable performance in terms of convergence time, with identification times of 13.54 and 14.01 seconds, respectively. However, the adaptive law achieves better parameter accuracy with an error of 6.1162×10^{-5}, compared with 1.5418×10^{-4} for gradient descent. Both methods show smooth convergence behavior in the simulation curves. The sliding mode adaptive method presents a trade-off between robustness and convergence speed. Although it requires the longest identification time of 18.02 seconds and exhibits the largest parameter error of 2.6378×10^{-4}, it achieves the second-best synchronization error of 2.1728×10^{-5}. The characteristic step-like chattering observed in Figure 16 reflects its inherent switching mechanism, which provides enhanced robustness against uncertainties at the cost of slower parameter convergence.

Table 1. Comparison of parameter identification methods.

Method	Identification time (s)	Parameter error	Synchronization time (s)	Synchronization error
Proposed method	11.52	9.9858×10^{-7}	11.77	1.5247×10^{-5}
Gradient descent [39]	13.54	1.5418×10^{-4}	13.79	2.2995×10^{-5}
Adaptive law [40]	14.01	6.1162×10^{-5}	13.83	2.3097×10^{-5}
Sliding mode adaptive [41]	18.02	2.6378×10^{-4}	13.82	2.1728×10^{-5}

To ensure a fair comparison among the four parameter-identification methods (Newton iteration, gradient descent, adaptive law, sliding mode adaptive), all synchronization-related settings were kept strictly identical across methods, so that any observed performance difference can be attributed solely to the identification law itself rather than to a more favorable control or network setting for one method. Specifically, (i) the hybrid impulsive controller and all its parameters (Υ, β, α, K, ν, $\tau_{\max}$, P) were fixed to the same values for every method, and the impulse instants $\{t_r\}$ were generated by the same deterministic rule and therefore occurred at identical times in all four simulations; (ii) the network topology set $\{Q^{(\omega)}\}$, the topology-switching signal $\omega(t)$, and the coupling strengths were generated once and reused identically across the four runs, rather than being regenerated per method, eliminating any bias from a particular random realization; (iii) all nodes were initialized with the same states $(x_i(0), y_i(0), z_i(0))$ and the same initial parameter estimates $\hat{a}_i(0)$ for every method; and (iv) parameter identification convergence and synchronization convergence were evaluated using the same numerical criteria (mean parameter error < 0.1 and mean synchronization error < 0.001, respectively) and the same clipping range $[0, 50]$ for all estimates. The only quantities that differed across methods were the identification-law-specific gains (e.g., the gradient-descent learning rate γ, the adaptive-law gain η and drift-suppression coefficient σ, and the sliding mode gains ρ, k_s, ϕ), each chosen within a commonly used range reported in the respective references so that no method was deliberately undertuned. Under these controlled conditions, the comparison in Table 1 isolates the effect of the identification mechanism, and the superior convergence speed and accuracy of the Newton–iteration method can be attributed to its use of second-order (Hessian-based) information rather than to any asymmetry in the experimental setup.

For the comparison study reported in Table 1, all four identification methods (Newton iteration, gradient descent, adaptive law, and sliding mode adaptive) used an identical hybrid impulsive controller with the same parameters Υ, β, α, K, $\tau_{\max}$, and ν as above, so that the only difference among the methods lay in the parameter identification law. The specific update laws and their exclusive parameters were as follows.

(i) **Gradient descent:**

$$\dot{\hat{a}}_i = \gamma \cdot \nabla_{\hat{a}_i} J, \tag{8.8}$$

where the gradient was evaluated as $-e_{x,i}(t)(y_i - x_i)$ and the learning rate was $\gamma = -0.8$.

(ii) **Adaptive law:**

$$\dot{\hat{a}}_i = \eta \cdot e_{x,i}(t)(y_i - x_i) - \sigma(\hat{a}_i - 10), \tag{8.9}$$

with the adaptation gain $\eta = 0.5$ and the parameter drift suppression coefficient $\sigma = 0.1$.

(iii) **Sliding mode adaptive:** The sliding surface was $s_i = e_{x,i}(t)$; the update law was

$$\dot{\hat{a}}_i = \rho|s_i| \cdot \mathrm{sign}(\hat{a} - \hat{a}_i) + k_s s_i(y_i - x_i), \tag{8.10}$$

with $\rho = 0.5$, $k_s = 0.6$, and boundary layer thickness $\phi = 0.8$ (saturation function used in place of the sign to reduce chattering).

In this comparison, the network used $N = 150$ nodes and a Lorenz system as the response/drive dynamics (parameters $a = 10$, $r = 28$, $b = 8/3$; target initialized at

$$(x_1(0), y_1(0), z_1(0)) = (2, 3, 0.1),$$

each response node was initialized at

$$(x_i(0), y_i(0), z_i(0)) = (1 - 0.1i, 1 + 0.2i, 0.2 + 0.3i),$$

the initial parameter estimates were $\hat{a}_i(0) = 10+i$). The total simulation time was $T_{\text{sim}} = 50$ s (5000 time steps at $h = 0.01$ s). Parameter identification convergence was declared when the mean parameter error

$$\frac{1}{N}\sum_{i=1}^{N} |\hat{a}_i - a| < 0.1,$$

synchronization convergence was declared when the mean synchronization error

$$\frac{1}{N}\sum_{i=1}^{N} \|e_i\| < 0.001.$$

Parameter estimates were clipped to $[0, 50]$ at each step to prevent nonphysical values.

In conclusion, the proposed method is recommended for applications requiring high precision and fast response, while the sliding mode adaptive method is preferable for scenarios demanding robustness under uncertain conditions.

9. Conclusions

This paper proposes a finite-time synchronization control method for CNNs with uncertain switching topologies via Newton iterative parameter identification. The hybrid impulsive controller achieves rapid and reliable synchronization through continuous-time regulation and discrete-time pulse correction. Theoretical analysis based on Lyapunov theory rigorously proves finite-time convergence with explicit time expressions, while simulation results on 15-node FHN networks demonstrate synchronization within 1 second under five randomly switching topologies. Compared with the gradient descent, adaptive law, and sliding mode methods, the Newton-iterative approach exhibits superior performance with a success rate of over 85%, attributed to superlinear convergence and automatic step-size adjustment. The method's key advantages include decoupling parameter estimation from synchronization dynamics, topology independence, and arbitrary switching capability.

Author contributions

Yongwei Yang: Writing—original draft, methodology, conceptualization, funding acquisition; Chengye Zou: Writing—review and editing, software, investigation; Hao Zhang: Supervision, investigation, software. All authors have read and approved the final version of the manuscript for publication.

Use of Generative-AI tools declaration

The authors declare they have not used artificial intelligence (AI) tools in the creation of this article.

Acknowledgments

This research is supported by the Post-doctoral Natural Science Foundation of China under grant number 2022M720650, the Start-up Fund Project of Talent Research in Tongling University under grant number 2025tlxyrc015, and the Special Research Project of the Provincial Scientific Research Platform of Tongling University under grant number 2025tlxyptZD31.

Conflict of interest

All authors declare no conflicts of interest in this paper.

References

1. O. Shobayo, R. Saatchi, Developments in deep learning artificial neural network techniques for medical image analysis and interpretation, *Diagnostics*, **15** (2025), 1072. https://doi.org/10.3390/diagnostics15091072
2. V. D. Vuong, L. H. Nguyen, J. A. Goulet, Coupling LSTM neural networks and state-space models through analytically tractable inference, *Int. J. Forecast.*, **41** (2025), 128–140. https://doi.org/10.1016/j.ijforecast.2024.04.002
3. H. Mohammadi, W. Karwowski, Graph neural networks in brain connectivity studies: methods, challenges, and future directions, *Brain Sci.*, **15** (2025), 17. https://doi.org/10.3390/brainsci15010017
4. W. B. Subait, N. Ahmad, M. S. A. Alzaidi, M. Alqahtani, A. A. Alhashmi, N. O. Aljehane, et al., Unveiling Arabic named entity recognition using natural language processing with artificial intelligence approach on Moroccan dialect, *Sci. Rep.*, **15** (2025), 30882. https://doi.org/10.1038/s41598-025-05940-y
5. Y. Cao, L. Zhao, Q. Zhong, K. Shi, J. Xiao, S. Wen, Synchronization of coupled neural networks with multiple switching topologies via adaptive control techniques, *Int. J. Robust Nonlinear Control*, **34** (2024), 8661–8675. https://doi.org/10.1002/rnc.7409
6. J. Wang, H. Wu, T. Huang, S. Ren, Finite-time synchronization and H_∞ synchronization for coupled neural networks with multistate or multiderivative couplings, *IEEE Trans. Neural Netw. Learn. Syst.*, **35** (2022), 1628–1638. https://doi.org/10.1109/TNNLS.2022.3184487
7. S. Tang, J. Li, H. Jiang, H. Jiang, Fixed-time aperiodic intermittent control for quasi-bipartite synchronization of competitive neural networks, *Entropy*, **26** (2024), 199. https://doi.org/10.3390/e26030199
8. Y. Huang, Y. Gao, L. Su, T. Wong, Predefined-time synchronization of coupled competitive neural networks, *Int. J. Adapt. Control Signal Process.*, **39** (2025), 609–621. https://doi.org/10.1002/acs.3961

9. A. Aili, S. Chen, S. Zhang, Event-triggered synchronization of coupled neural networks with reaction-diffusion terms, *Mathematics*, **12** (2024), 1409. https://doi.org/10.3390/math12091409
10. X. Zheng, J. Wang, K. Shi, X. Cai, Y. Tang, Intelligent hybrid event-triggered synchronization control of delayed neural networks with actuator failure via semi loop functional, *Discrete Contin. Dyn. Syst. Ser. S*, **18** (2025), 2429–2447. https://doi.org/10.3934/dcdss.2024139
11. C. Yi, J. Cai, R. Guo, Synchronization of a class of nonlinear multiple neural networks with delays via a dynamic event-triggered impulsive control strategy, *Electron. Res. Arch.*, **32** (2024), 4581–4603. https://doi.org/10.3934/era.2024208
12. C. Zheng, J. Yu, F. Kong, C. Hu, Fixed-time synchronization of discontinuous fuzzy competitive neural networks via quantized control, *Fuzzy Sets Syst.*, **482** (2024), 108913. https://doi.org/10.1016/j.fss.2024.108913
13. W. Chen, H. Li, Complete synchronization of delayed discrete-time fractional-order competitive neural networks, *Appl. Math. Comput.*, **479** (2024), 128872. https://doi.org/10.1016/j.amc.2024.128872
14. T. Li, H. Li, X. Fan, L. Zhang, Complete synchronization of discrete-time fractional-order Cohen–Grossberg networks with time delays via adaptive nonlinear controller, *Math. Methods Appl. Sci.*, **48** (2024), 4708–4722. https://doi.org/10.1002/mma.10571
15. Z. Wu, D. Yang, H. Li, Y. Yu, X. Liu, P. Cattani, et al. A novel event-dependent intermittent control for synchronization of fractional-order coupled neural networks with mixed delays and higher-order interactions, *Fractal Fract.*, **9** (2025), 824. https://doi.org/10.3390/fractalfract9120824
16. X. Zhou, J. Cao, Z. Guan, X. Wang, F. Kong, Fast synchronization control and application for encryption-decryption of coupled neural networks with intermittent random disturbance, *Neural Netw.*, **176** (2024), 106404. https://doi.org/10.1016/j.neunet.2024.106404
17. Q. Chang, R. Wang, Y. Yang, Finite-time cluster synchronization of fractional-order complex-valued neural networks based on memristor with optimized control parameters, *Fractal Fract.*, **9** (2025), 39. https://doi.org/10.3390/fractalfract9010039
18. L. Liu, H. Bao, J. Cao, Fixed-time event-triggered impulsive secure synchronization of quaternion-valued fuzzy neural networks subject to stochastic cyber-attacks, *IEEE Trans. Fuzzy Syst.*, **33** (2025), 559–569. https://doi.org/10.1109/TFUZZ.2024.3485515
19. X. Chen, T. Jia, Z. Wang, X. Xie, J. Qiu, Practical fixed-time bipartite synchronization of uncertain coupled neural networks subject to deception attacks via dual-channel event-triggered control, *IEEE Trans. Cybern.*, **54** (2024), 3615–3625. https://doi.org/10.1109/TCYB.2023.3338165
20. X. Si, Z. Wang, X. Huang, H. Shen, Resilient sampled-data control for bipartite synchronization of cooperation-competition neural networks against denial-of-service attacks, *IEEE Trans. Autom. Sci. Eng.*, **22** (2025), 17778–17789. https://doi.org/10.1109/TASE.2025.3585403
21. J. Han, Finite-time passivity and synchronization for a class of fuzzy inertial complex-valued neural networks with time-varying delays, *Axioms*, **13** (2024), 39. https://doi.org/10.3390/axioms13010039

22. Q. Cui, J. Cao, M. Abdel-Aty, A. Kashkynbayev, Global practical finite-time synchronization of disturbed inertial neural networks by delayed impulsive control, *Neural Netw.*, **181** (2025), 106873. https://doi.org/10.1016/j.neunet.2024.106873
23. J. Ran, T. Zhang, Fixed-time synchronization control of fuzzy inertial neural networks with mismatched parameters and structures, *AIMS Math.*, **9** (2024), 31721–31739. https://doi.org/10.3934/math.20241525
24. C. Chenthamarakshan, S. Ganesan, K. Sivakumar, A. Kashkynbayev, Quasi-bipartite synchronization for delayed coupled inertial neural networks having cooperative and competitive communication via pinning control strategy, *IET Control Theory Appl.*, **19** (2025), e12780. https://doi.org/10.1049/cth2.12780
25. P. B. Dhivakaran, A. Vinodkumar, S. Vijay, S. Lakshmanan, J. Alzabut, R. A. El-Nabulsi, et al., Bipartite synchronization of fractional order multiple memristor coupled delayed neural networks with event triggered pinning control, *Neural Process. Lett.*, **56** (2024), 50. https://doi.org/10.1007/s11063-024-11507-1
26. S. Dong, K. Shi, S. Wen, Y. Shen, S. Zhong, Almost surely synchronization of directed coupled neural networks via stochastic distributed delayed impulsive control, *Chaos Solitons Fract.*, **174** (2023), 113742. https://doi.org/10.1016/j.chaos.2023.113742
27. H. Q. Wu, X. Q. Zhao, L. Y. Wang, J. D. Cao, Observer-based fixed-time topology identification and synchronization for complex networks via quantized pinning control strategy, *Appl. Math. Comput.*, **507** (2025), 129568. https://doi.org/10.1016/j.amc.2025.129568
28. Y. Li, Q. M. Zhu, J. H. Zhang, Adaptive fixed-time neural networks control for pure-feedback non-affine nonlinear systems with state constraints, *Entropy*, **24** (2022), 737. https://doi.org/10.3390/e24050737
29. G. Zhang, S. Wen, New approximate results of fixed-time stabilization for delayed inertial memristive neural networks, *IEEE Trans. Circuits Syst. II Express Briefs*, **71** (2024), 3428–3432. https://doi.org/10.1109/TCSII.2024.3361670
30. X. Ma, C. Hu, J. Yu, S. Wen, L. Wang, Y. Sheng, Hyperbolic function-based limited-time stability and limited-time synchronization for fuzzy switched Cohen-Grossberg neural networks, *Nonlinear Dyn.*, **114** (2026), 597. https://doi.org/10.1007/s11071-026-12469-w
31. K. Xiong, C. Hu, J. Yu, L. Wang, Special function-based limited-time synchronization of multilayered coupled quaternion networks, *Commun. Nonlinear Sci. Numer. Simul.*, **145** (2025), 108694. https://doi.org/10.1016/j.cnsns.2025.108694
32. Q. Xi, X. Z. Liu, X. D. Li, Finite-time synchronization of complex dynamical networks via a novel hybrid controller, *IEEE Trans. Neural Netw. Learn. Syst.*, **35** (2024), 1040–1049. https://doi.org/10.1109/TNNLS.2022.3185490
33. J. Fang, N. N. Yin, D. Wei, H. Liu, W. Deng, Improved finite-time synchronization of coupled discontinuous neural networks under adaptive sliding mode control, *Int. J. Dyn. Control*, **12** (2024), 396–408. https://doi.org/10.1007/s40435-023-01202-9
34. L. Dai, Z. Liu, H. Xu, Y. Zhang, Novel finite-time convergent neural dynamics for practical synchronization of diverse chaotic systems, *Commun. Nonlinear Sci. Numer. Simul.*, **151** (2025), 109122. https://doi.org/10.1016/j.cnsns.2025.109122

35. Q. Cui, J. D. Cao, M. Abdel-Aty, Finite-time bipartite synchronization for coupled neural networks: An aperiodically intermittent and impulsive control approach, *Expert Syst. Appl.*, **290** (2025), 128433. https://doi.org/10.1016/j.eswa.2025.128433

36. C. Hu, J. Yu, Z. Chen, H. Jiang, T. Huang, Fixed-time stability of dynamical systems and fixed-time synchronization of coupled discontinuous neural networks, *Neural Netw.*, **89** (2017), 74–83. https://doi.org/10.1016/j.neunet.2017.02.001

37. R. A. Horn and C. R. Johnson, *Matrix analysis*, Cambridge: Cambridge University Press, 2012. https://doi.org/10.1017/CBO9780511750922.006

38. X. D. Li, D. W. C. Ho, J. D. Cao, Finite-time stability and settling-time estimation of nonlinear impulsive systems, *Automatica*, **99** (2019), 361–368. https://doi.org/10.1016/j.automatica.2018.10.024

39. D. E. Rumelhart, G. E. Hinton, R. J. Williams, Learning representations by back-propagating errors, *Nature*, **323** (1986), 533–536. https://doi.org/10.1038/323533a0

40. J. J. E. Slotine, W. Li, *Applied nonlinear control*, Englewood Cliffs, NJ: Prentice hall, 1991.

41. V. I. Utkin, Sliding mode control design principles and applications to electric drives, *IEEE Trans. Ind. Electron.*, **40** (1993), 23–36. https://doi.org/10.1109/41.184818

AIMS Press

© 2026 the Author(s), licensee AIMS Press. This is an open access article distributed under the terms of the Creative Commons Attribution License (https://creativecommons.org/licenses/by/4.0)